Property-based functional gradients for biomimetic composites

Robin Petrus Elias Veeger

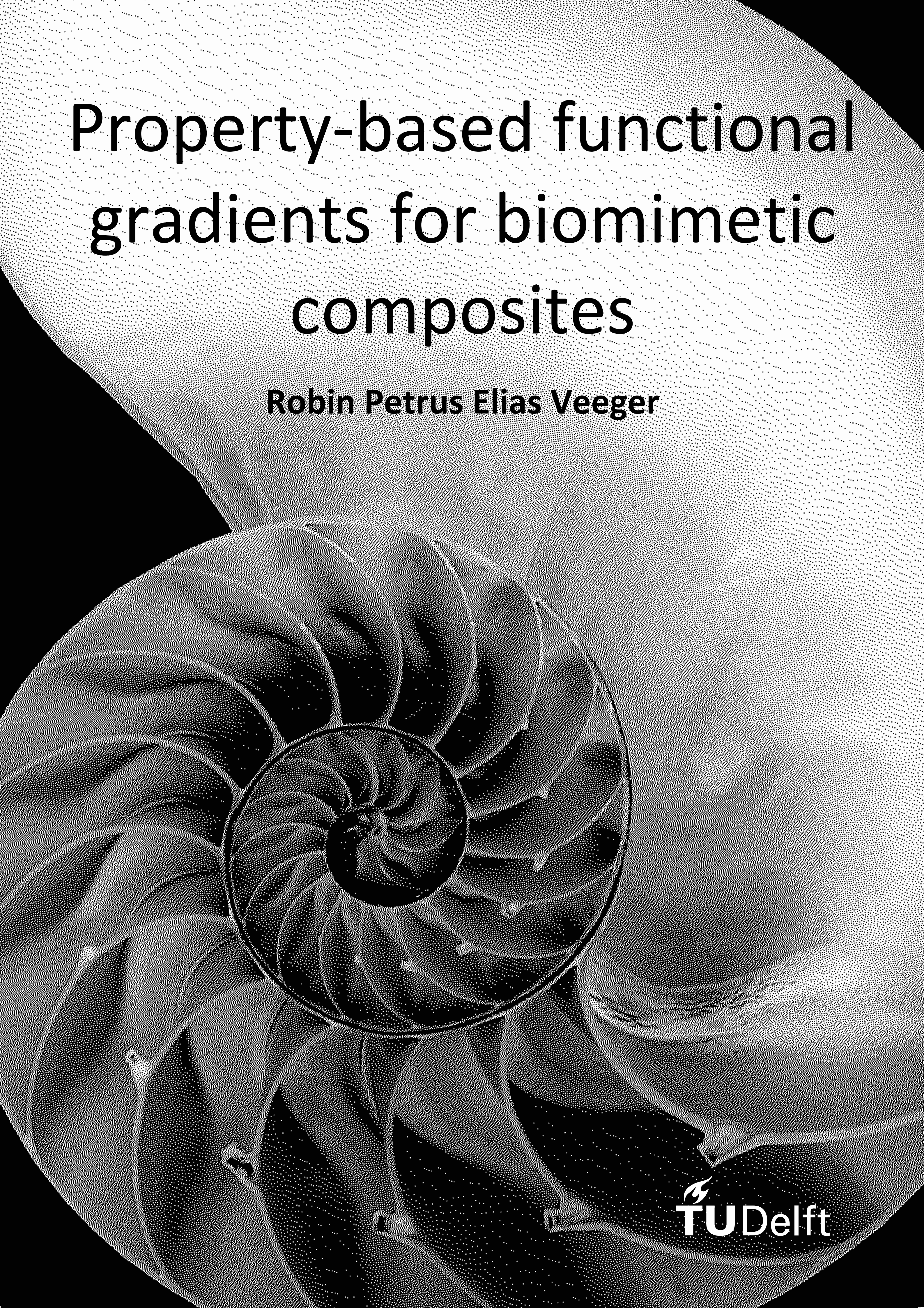

TU Delft

Property-based functional gradients for biomimetic composites

By

Robin Petrus Elias Veeger

in partial fulfillment of the requirements for the degree of

Master of Science
in Biomedical Engineering

at the Delft University of Technology,
to be defended publicly on Friday, November 26, 2021, at 10:00 AM.

Student number:	4302931	
Supervisor:	Dr. M. J. Mirzaali	
	Prof. dr. A. A. Zadpoor	
	Prof. D. Ruffoni	
Thesis committee:	Prof. dr. A. A. Zadpoor,	TU Delft
	Dr. S.T. Abrahami,	TU Delft
	Dr. M. J. Mirzaali,	TU Delft
	M. C. Saldivar,	TU Delft

This thesis is confidential and cannot be made public until December 31, 2023.

Disclaimer:

In this report, I chose to use the “we” format as reporting style in consultation with my supervisors. This choice was based on the intention to in the future maybe publish (parts of) this work and therefore stay as close as possible to the reporting style for such a publication. The responsibility for the content of this work lies by me, as it is the reflection of the graduation project research that I performed independently, coached by my supervisors.

Sassenheim, 16 november 2021

Robin Veeger

Abstract

Functional gradients in hard-soft interfaces are abundant in nature, and we often mimic them to create strong and tough composites. A powerful tool for the designs and fabrication of biomimetic composites is voxel-based multi-material 3D printing. Earlier researches mainly focused on using this technique in the creation of gradients based on morphology. While this is a great way to create a gradient, the outcome material properties are often unknown. In this research, we attempted to create a gradient based on the desired outcome material properties rather than morphology. We created a linear gradient in density using a voxel-based 3D printing technique and tested it through nanoindentation. Furthermore, we created a Finite Element Model based on this sample. Out of the nanoindentation and Finite Element Model results, we extracted the b-value for a power-law function in the form of $E(x) = E_h\rho(x)^b + E_s$. With the inverse of this power-law function, we designed three different gradients based on the desired material properties: a linear, stepwise, and sigmoid gradient. Nanoindentation experiments and Finite Element analyses showed that we achieved the desired outcome in material properties with our newly created approach of designing gradients. However, the nanoindentation experiments showed that using a machine suitable for the wide range of Young’s moduli present in these kinds of composites is crucial. To display the possible applications of our new approach, we designed a knee model with graded ligaments and tested it with a tensile test and digital image correlation. Results of these tests showed an energy before failure that was twice as high as its non-graded counterpart. Furthermore, with the introduction of the gradient, we achieved to change to loading condition on the ligaments. Overall, our results show that our new approach can create gradients based on material properties rather than morphology and opens many new doors in creating biomimetic composites.

Acknowledgments

After three wonderful years at the TU in Delft, this thesis represents everything I have learned during this time. It was a great and very educational experience where I have been introduced to a, for me, exciting new research field. However, it was also tough given the sudden changes in the world due to Covid. Of course, I have not gone through this graduation alone, so I would like to thank everyone evolved in this project.

First, I would like to thank my weekly supervisor Mohammad Mirzaali for introducing me to the research group, his support in setting up the project, and his helpful feedback and guidance throughout the process. I am very grateful for his excellent advice and that I could be part of this group.

I would like to thank my professor Amir Zadpoor for introducing me and providing me an opportunity to work on this fascinating subject and his guidance throughout the project.

I would like to thank Davide Ruffoni for his always helpful feedback throughout the project and his assistance and guidance in performing the nanoindentation experiments.

A special thanks to Mauricio Saldivar for his daily supervision, input, and feedback throughout the project, assistance in 3D printing the samples, and advice during the many complications I had in this project. Without his support, the project could not have been what it is right now.

I would like to thank Edwin Tay for his helping hand during the pre-processing of the samples and the nanoindentation experiments, especially when we had to make a sudden switch between indentation machines.

Finally, I would like to thank my family and friends for supporting me during this process. I could not have done it without their love and support.

Robin Petrus Elias Veeger
Sassenheim, November 2021

Contents

1. Introduction

1.1. Bioinspired approach for an improved mechanical performance

In artificial composites, strength and toughness often come at the cost of each other. Furthermore, hard-soft interfaces in engineered materials are usually susceptible to failure. The reason that strength and toughness are mostly mutually exclusive is how a material achieves its properties. Literature defines strength as the ability of a material to withstand an applied load and uses different measurement methods for this. Which are the applied load before plastic deformation (yield strength) and the applied load before complete failure (ultimate load). On the other hand, toughness is the ability of a material to absorb energy without fracture [1]. Strong materials are often brittle, while tough materials are compliant. An example of strong material is a steel beam, while an extremely tough material would be a rubber band. There are examples of artificial materials that have both, such as bulletproof vests [2]. However, these cases are exceptional. Since the combination of strength and toughness is challenging to achieve, a decision often has to be made between the two, depending on the purpose of the material. In a situation where catastrophic failure is unacceptable, tougher materials often have the preference. However, ideally, strength and toughness are combined. Because of this, research on combining these material properties is necessary.

In nature, we observe the contrary to artificial materials. Natural materials are evolved and adapted so that both strength and toughness are present. Many years of evolution are underlying for these exceptional mechanical performances. Over the past millions of years, constant adaptation resulted in strong and tough composites. A reason for failure in artificial materials is the presence of high interface stresses. These high interface stresses result from a significant mismatch in Young's moduli of two material phases [3]. Nature counteracts this mismatch problem by creating different gradients and hierarchical structures between the two material bodies, acting on multiple length scales [4]. The gradients can be smooth, as seen in the muscle-tendon interface, or discontinuous, as seen in nacre. Both types of gradients reduce the chance of failure by reducing the stress concentrations at the interface [5].

However, we can distinguish between smooth and discontinuous gradients and between one or multiple material bodies. In nature, gradients can be present within one material body, such as found in nacre and bone (Figure 1A-B) [6]–[8], or between different material bodies, such as seen in the bone-tendon and muscle-tendon interface (Figure 1C) [9], [10]. Furthermore, the muscle-tendon interface is an example of a smooth and nacre of a discontinuous gradient. A high mismatch between Young's moduli exists in these gradients. A great example of this is the bone-tendon interface in the human gastrocnemius. The Young's modulus of the bone is around 35 (GPa), whereas that of the tendon is approximately 1.2 (GPa) [11]–[13]. The increase in material properties can be a result of toughening mechanism implemented in a composite. Nature has found several ways to do this, and we can find great examples of this inside nacre and bone. In nacre and bone, cracks get deflected and arrested due to toughening mechanisms [14], [15]. Because of these mechanisms, nacre and bone are significantly stronger than their constituent materials.

Another excellent example of a hard-soft interface found in nature is inside of the bone at the sub-nanoscale. At this scale, bone consists of two main constituents: a collagen matrix and hydroxyapatite crystals inside this matrix (Figure 1D). There is a significant difference in Young's modulus between the constituents. Collagen has Young's modulus of around 1-2 (GPa), while the hydroxyapatite crystals have Young's modulus of about 100-150 (GPa) [16]. The two constituents have their own mechanical role. The collagen matrix dissipates energy under mechanical deformation, while the hydroxyapatite crystals provide the load-bearing capacity [17]. The structure of collagen and hydroxyapatite crystals in bone is well understood and inspired plenty of biomimetic designs. Among many [18]–[22], studies like Dimas et al. [23] recreated the morphology found in bone using 3D printing techniques and showed that this significantly increases the mechanical fracture characteristics.

Studies have not only used the hydroxyapatite crystals in biomimetics based on bone. Sedighi et al. [24] used hydroxyapatite crystals inside a titanium mixture at different volume ratios to create a dental implant with a functional gradient (Figure 1E). Their study showed an optimum ratio between titanium and hydroxyapatite crystals, which gives the highest Vickers microhardness. While Sedighi et al. [24] did create a functional gradient inside an implant, they did not investigate the main challenge with dental implants. The mismatch of material properties between the dental implant and the biomaterial is a big issue. Osseointegration becomes challenging when the mismatch is too big. Sadollah et al. [25] did investigate this problem. In their study, they created a dental implant with a gradient. Using different optimization criteria, they showed that the optimal gradient design is different for the different criteria. For the ingrowth of bone, a steeper drop in Young's modulus is desirable. However, this is not the best shape for the overall stiffness of the implant, for which a less steep drop is desirable. This research showed that a gradient is beneficial for bone ingrowth and implant stiffness. Nevertheless, they also showed that it is challenging to find the best gradient for different design criteria, and thus, the design criteria should always be kept in mind.

The earlier mentioned examples of materials in which we used gradients are all from the biological side of the literature. However, of course, there are examples present where we use gradients that are not biological. Gradients, whether or not biomimetic, can be used in many other applications. One of those is graded concrete (Figure 1F). Construction workers can use graded concrete while building structures to enhance their mechanical behavior. Studies show that tall buildings, whose framework included graded concrete, show less sway on the upper floors when placed under a lateral load. This is important because graded concrete will introduce a more rigid response to, for example, earthquakes [26]. Another example of a structure where we use a gradient to overcome a problem in our daily lives is in the blades of an aircraft turbine (Figure 1G). In order to tackle the high thermal impact the blades have to overcome, the blades are made of a combination of metal interior and a ceramic outer layer [27]. However, without using a gradient between these two phases, the adhesion is insufficient, resulting in failure. Introducing a gradient between the phases performs better under several different loading conditions, making it crucial for enhancing the mechanical performances of the blade [28]. These two examples show that we can learn from gradients found in nature and implement them in a wide variety of applications to enhance their performances.

From these examples, we can conclude that functional gradients and hierarchical structures are crucial for combining strength and toughness. We can use these features as an inspiration for creating new composites, and doing so is a very modern approach for engineering materials. To understand and apply some of the main characteristics of these graded structures, accurate selection of manufacturing method, design methodology, and proper testing and analysis are fundamental steps for bringing high-performing structures into our daily lives. The examples, such as the turbine blades, show that we use gradients in our daily lives for non-biological applications. However, further investigation in gradients can be beneficial for many more, ranging from the medical field to daily used materials. We can perform this investigation in several ways, and two of them are through additive manufacturing and finite element modeling. We will discuss the state of the art of these techniques in the next chapter.

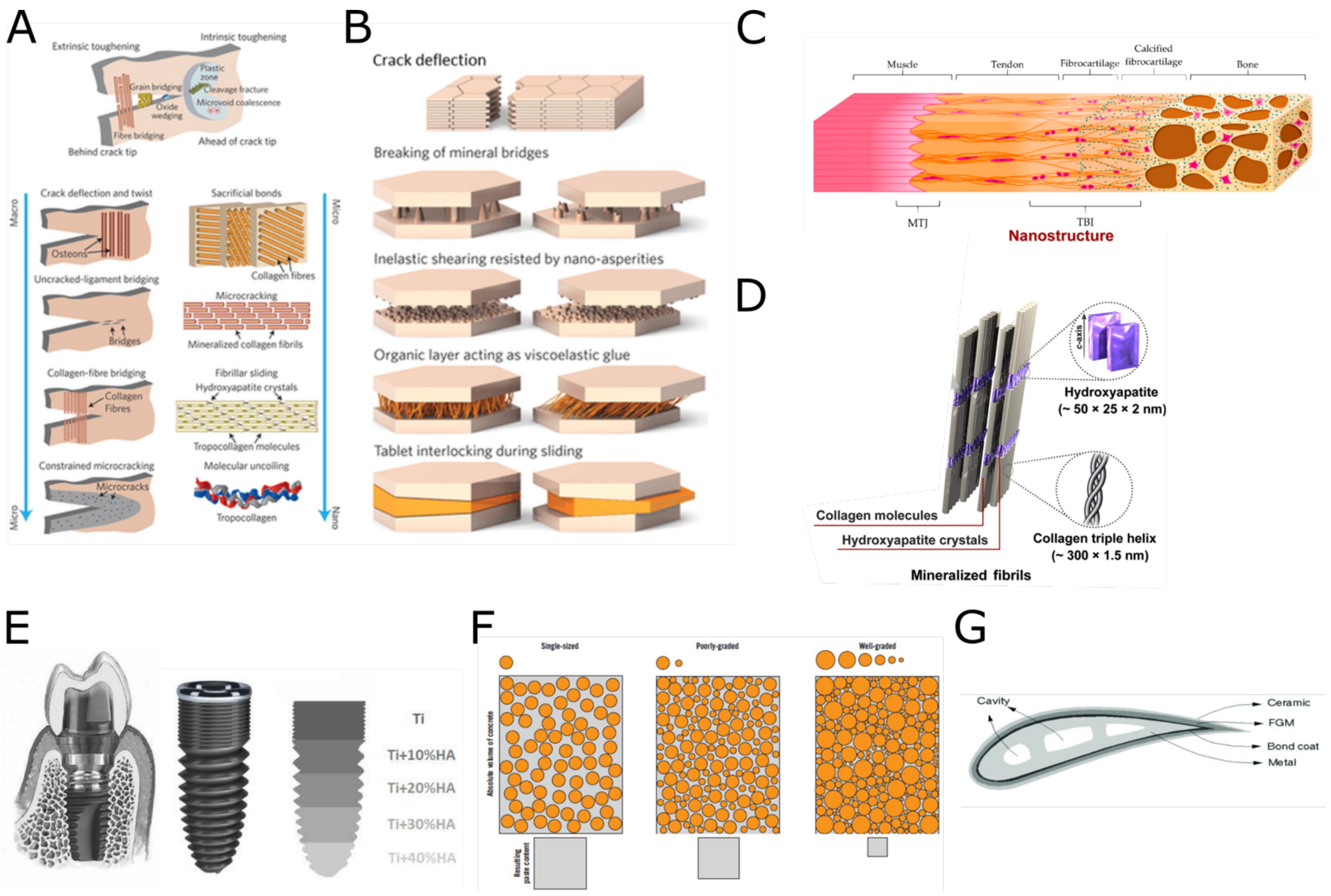

Figure 1: A) Several toughening mechanisms found in bone and B) found in nacre. Taken from Libonati & Buehler [8]. C) Gradients found inside a muscle-bone-tendon interface. Taken from Bianchi et al. [29]. D) Schematic view of graded concrete. Taken from CivilWeb Spreadsheets [30]. E) Schematic view of hydroxyapatite crystals inside the collagen matrix. Adjusted from Sadat-Shojai et al. [31]. F) Left: view of a dental implant inside the jaw. Adjusted from Sadollah et al. [25]. And right: schematic view of a titanium hydroxyapatite gradient inside the implant. Taken from Sedighi et al. [24]. G) Schematic view of a functional gradient inside a turbine blade. Adjusted from Bhavar et al. [27].

1.2. State of the art in additive manufacturing and Finite element method

Additive manufacturing (AM) techniques are widely used in the literature to mimic nature's gradients and hierarchical structures. We can use them as an inspiration for creating composites deriving from them. Techniques such as 3D printing [19], freeze casting [32], [33], layer-by-layer deposition [34]–[36], electrophoretic deposition [37], mechanical assembly [38] and self-assembly [39], [40] have been used to create composites based on materials found in nature [41], [42]. With AM, creating more complex structures and gradients is possible, which is impossible with traditional manufacturing techniques. Furthermore, with AM, it is also possible to print different materials simultaneously to create designs. With this multi-material 3D printing, we can use materials with completely different material properties. This technique is especially suitable to mimic structures with extreme differences in properties between different materials, such as the example of hydroxyapatite crystals inside a collagen matrix.

A reasonably novel multi-material 3D printing technique is called voxel-based 3D printing. Voxels refer to a volumetric pixel, in other words, a 3D pixel. The most common shape of these pixels is a cube or rectangle. 3D printers can, with the use of a voxel-by-voxel approach of printing, create complex gradients and hierarchical structures on multiple length scales within a structure [43]. In contrast to other additive manufacturing methods, voxel-based 3D printing uses bitmap files instead of STL files. Because this technique uses bitmap files, it can achieve a higher control and accuracy of the deposition of different materials [44]. These properties make this method exceptionally suitable for creating complex gradients and structures between different materials while achieving a high resolution.

Another way to study gradients and structures is through Finite Element Modeling (FEM). FEM is widely used to analyze and evaluate a structure mechanically. Doing this is fundamental for understanding the mechanical influences of the introduction of gradients into structures. With FEM, one can perform complicated calculations about the mechanical properties of intricate materials that would be too complex to calculate analytically. Besides, with FEM, it is easier to assess in a non-invasive way which design parameters affect the overall performances of a designed composite. A researcher can easily adjust separate parameters to investigate how they influence the material's behavior without the need for physical prototypes. Besides this, with FEM, it is easier to study many intricate designs. Furthermore, better visualization of the mechanical response of the structures can be achieved, which would generally be impossible to study in an experimental setup. Another advantage is that any design artifacts that the 3D printing process could introduce are not present. Finally, researchers can infinitely repeat experiments performed with FEM without needing a 3D printer to create new samples. Because the computers used for the FEM are rapidly getting better and more powerful, FEM is a fast-growing research field. Over the past years, researchers have been able to design and test increasingly more complicated designs. All these properties of FEM make it an excellent tool to use in creating and studying gradients and other hierarchical structures. Because of the advantages mentioned above, both FEM and AM are widely used to study gradients [45]–[47].

Because AM techniques and FEM are valuable tools to study and mimic graded structures to create strong and tough composites, for the next part, we will discuss the literature regarding the state of the art of additive manufacturing of bioinspired structures and their Finite Element analysis. Furthermore, we will review other techniques to study gradients and ways to predict the mechanical properties of hard-soft gradients.

1.3. State of the art in bioinspired design and voxel-based manufacturing

In recent years, much research has proven many applications and potential for multi-material AM and bioinspired design to work in synergy to improve our architected materials. We know these techniques subdivide into graded structures, hierarchical design, crack deflecting structures, suture, or enthesis design [6]–[10], [14], [15], [26], [27]. Here some of the most relevant literature will be reviewed that studied these structures using AM techniques and FEM. Furthermore, we will also investigate which models are currently used to predict the properties of hard-soft composites.

Many gradients and structures found in the literature are based on natural examples. The hard-soft interfaces found in nacre are widely studied and implemented in different applications [48], [49]. Studies that created bioinspired morphologies found several mechanisms that result in a strong and tough composite. The brick-and-mortar structure of the nacre introduces these mechanisms. The way a crack propagates through a brick-and-mortar-like structure is dependent on the hierarchical architecture [23]. Implementing soft layers inside a rigid composite can significantly enhance the overall toughness by increasing the crack path [50]. The brick-and-mortar structure also introduces other mechanisms, such as organic matrix bridging between the platelets [51], [52], interlocking of the platelets [4], [7], [14], and crack bridging [53], [54]. We can find the same kinds of mechanisms inside the bone. Studies that mimic the hierarchical structure of bone, such as that of Dimas et al. [23] and Libonati et al. [55], found several toughening mechanisms introduced by the morphology of bone that is somewhat similar to those in nacre. A great example of this is the way a crack propagates through a bone-like structure. Different studies on 3D printed samples based on nacre and bone show that the cement line in bone acts in the same way as the organic layer in nacre [15], [23], [54]; they both deflect a crack, which results in a longer crack path and more energy dissipation. Overall, crack deflection, strain delocalization, and bridging are some of the mechanisms that make nacres and bone architectures unique. Understanding how nature accomplishes these mechanisms and being able to mimic and implement them is crucial in creating tough composites.

More examples in nature show that a gradient between two material bodies is necessary for the material to be strong and tough. One of those is the enthesis. The gradient between tendon or ligament and bone can be studied and mimicked to investigate its influence. McCorry et al. [56] did this. In their study, they created a new method to create a simplified enthesis and test the collagen integration with bone. As they created the enthesis, they either fixated the ends or did not. The collagen formed fibers in the longitudinal direction in the fixated samples and created a gradient within the material. As expected, this gradient resulted in five times higher elastic modulus in a tensile test than the non-fixated samples. This shows that a gradient between the hard bone and soft tendon is crucial for its function inside the body. Furthermore, McCorry et al. [56] showed that the direction of the collagen fibers in the gradient is vital for the increase of toughness. When one creates an artificial gradient, one should consider this effect. A gradient will only function well if its direction is correct. Boys et al. [57] confirmed that this gradient is critical for the tough bone-to-tissue interaction. They investigated the structural and mechanical features of the attachment site of the meniscus to the bone. Their technique clearly distinguished a stiff region consisting of open and dense trabecular bone, a homogeneous compliant region consisting of disorganized fiber bundles, and a heterogeneous compliant region consisting of oriented fiber bundles. These different regions create a mechanical gradient within the hard-soft interface, and when these regions work together, they successfully dissipate energy without localizing stresses. These results again show us that a gradient is necessary to toughen a hard-soft interface and that different morphologies of the used materials can introduce such a gradient. Furthermore, they also showed that a region with organized fibers is essential for an effective gradient.

Research has discovered many essential effects when designing gradients. This is especially the case for studies that have dealt explicitly with functional gradients. One of the main challenges of designing functional gradients is the capacity for our multi-material machines to define a continuous spectrum of material properties. Kokkinis et al. [58] performed another approach to study the influence of gradients on a material's overall mechanical performances. They created a multi-material 3D printing platform for 3D printing gradients by combining two resins in different proportions. This mixing can achieve thirteen different material combinations, with a range in Young's modulus of three orders of magnitude [58]. Although they only looked into two relatively simple stepwise gradients (ascending and descending) and a soft layer between a stiff and compliant material, they showed that an ascending stepwise from stiff to compliant and a soft layer between the materials could significantly improve the failure strain. The ascending stepwise and the soft layer move the strain energy density away from the stiff-compliant interface. This increases the material's overall strength as the replacement of the strain energy density reduces the stress concentration at the stiff interface. With their method, the authors show that they can adjust the strain energy density and create a composite with a tunable failure.

The study of Kokkinis et al. [58] used a multi-material approach of 3D printing to investigate gradients. However, the resolution they could achieve was much lower than that with a voxel-based approach. They printed with a layer thickness of 300 (μm), whereas with voxel-based 3D printing, a layer thickness of 14 (μm) is possible. Furthermore, with their setup, they could not print each material pure. To achieve this, they needed an extra print nozzle. With a similar approach, while using bitmap printing, the mixture of the materials is infinite, rather than stepwise combinations, as seen in their study. Because of this, it is essential to further look into the literature for studies where they did use a voxel-based 3D printing approach to investigate gradients.

Kaweesa et al. [59] did use a voxel-based 3D printing approach. They used this technique to investigate the influence of different gradients on the fatigue life in tensile samples. They created four different gradients between a hard and soft polymer: two linear and two stepwise. The authors tested the samples in a loading and relaxation cycle until failure. Both gradients showed results that are worse than that of the control gradient. As the transition region increased, the fatigue life of the samples decreased. However, the samples failed at the soft material region. The authors note that the reason behind this is the way that they designed the gradients. In this study, the authors assumed that the material would show an elastic behavior in the regions in the gradient where the number of soft material voxels would outnumber that of the hard. However, they found that this is not the case, as the elastic region of the linear and stepwise samples is much smaller than that of the control samples. This increases the stress concentrations at the soft region and decreases the fatigue life. Nevertheless, their study found that the stepwise gradients increased fatigue life compared to the linear gradients. This means that considering graded transitions is still fundamental for improving the fatigue-life cycle of multi-material structures.

Hasanov et al. [60] further studied the effect of a gradient in a tensile sample on the material's overall strength. Using voxel-based 3D printing, they created a linear gradient inside a sample and compared it to a direct transition from hard to soft. The graded sample showed an overall increase in Young's modulus of 25% and tensile strength that was twice as high. These results show that a gradient can successfully enhance the material properties of a composite. Mirzaali et al. [61] found similar results. They found that Young's modulus of graded tensile samples with a continuous gradient was three times higher than that of a no gradient control sample. For stepwise gradients, they only found that the Young's modulus increases with a higher number of steps. This suggests that the number of steps greatly influences the material properties of such a gradient. However, there is a trade-off to the increase in Young's modulus, as toughness and elongation decreased in the samples. These results show that we can tune the material properties of a composite by introducing gradients.

Overall, several studies have explored and mimicked gradients to study their influence on material properties. Besides the methods mentioned above, we can find models in the literature to predict the material properties. One of them is the Halpin-Tsai model. The Halpin-Tsai model is a classic approach and is mainly used to predict the elastic modulus of a composite reinforced with short fibers. The Halpin-Tsai equation is the following [62]:

$$E_c = E_m \left(\frac{1 + \zeta \eta V_f}{1 - \eta V_f} \right) \tag{1}$$

Wherein E_c is the elastic modulus of the composite, E_m the elastic modulus of the matrix, ζ is a parameter based on the geometry of the fibers, often in the range from 0 to 2 [63], V_f the volume fraction of the fibers and η is calculated by:

$$\eta = \frac{\frac{E_f}{E_m} - 1}{\frac{E_f}{E_m} + \zeta} \tag{2}$$

In this equation, E_f is the elastic modulus of the fibers.
In theory, this model should be applicable to simple voxel-based 3D printed structures since we can consider the hard voxels as particles distributed inside the composite. However, the Halpin-Tsai model does assume that the composite is reinforced with parallel aligned short fibers [64], which is not necessarily the case with voxel-based 3D printing. So, further study is necessary to examine if we can use the Halpin-Tsai model in this case.

Besides the Halpin-Tsai model, there are other models present to predict the material properties. Another section of composites by design is the bone power-law models. In the literature, we can find several models, such as that of Morgan et al. [65], Keyak et al. [66], Rice et al. [67], Hvid et al. [68], and Carter and Hayes [69]. The different bone power-law functions all have the form of:

$$E = a\rho^b \tag{3}$$

Wherein E is Young's modulus, ρ the apparent density, and a and b constants that we can characterize from physical tests. However, all earlier mentioned studies found different values for a and b, resulting in slightly different equations. These power-law functions have the advantage that with most of them, only the bone density has to be known, making it easier to use compared to the Halpin-Tsai model. Researchers have used power-law functions in other applications than bone. Kantaros et al. [70], for example, used them to predict the material properties of lattice structures. They used an equation based on a power-law model created by Gibson & Ashby [71] with the following shape:

$$\frac{E_{eff}}{E} = C_1 \left(\frac{\rho_{sc}}{\rho_0} \right)^2 \tag{4}$$

Wherein E is the elastic modulus of the solid part, $\mathrm{E_{eff}}$ the elastic modulus of the cellular structure, $\mathrm{C_1}$ a constant related to the structure's geometry, which we can obtain by fitting this formula to experimental data, and $\frac{\rho_{sc}}{\rho_0}$ the relative density of the cellular structure. They used a derivate of this formula to describe a decreasing trend in mechanical properties seen in porous scaffold structures when porosity increases. A comparison between the experimentally gathered data and the ones predicted by the equation showed that the predicted data followed the same pattern as the experimental data, although there was a slight underestimation. In theory, we could use these power-law functions to predict the properties of bitmap printed structures. However, little exploration on this subject exists.

In the above section, several models were discussed to predict the material properties of composites and showed that studies applied them to several applications. However, as said before, they have not yet been applied to bitmap 3D printed structures. Because of this, further research is necessary to investigate if these models correctly predict the material properties of composites created with this technique. We can do this by combining Finite Element models and experimental testing of additive manufactured structures and investigating which models work and which do not.

1.4. Fundamental next steps

Overall, gradients have proven to be a fundamental necessity when one introduces structures with extreme material phases. From examples found in nature, such as nacre and bone, we know that the hierarchical structure of the material can introduce toughening mechanisms. Studies regarding the enthesis show that fibers of collagen create a stronger material. Several material phases from bone to tendon are underlying to the enthesis's ability to dissipate energy. From studies on multi-material 3D printing, we know that stepwise gradients between a stiff and compliant material can increase a material's overall strength and fatigue life. However, a continuous gradient, such as a linear one, increases Young's modulus and tensile strength of a composite even more than a discontinuous one. Nevertheless, an input morphological gradient would not necessarily result in a one-to-one representation of material properties in the printed sample [59]. Just as with the other earlier mentioned studies, Kaweesa et al. [59] created a gradient based on morphology and investigated if, and in what way, this will result in a tougher composite. An intriguing discussion is whether the mechanical properties in materials found in nature result from morphology or the other way around. One could conclude that it is more logical to say that the morphology results from the function required of material in nature. Therefore, there is a fundamental necessity in designing methodologies that allow us to design materials based on property, regardless of the internal architecture that provides the gradients.

Furthermore, most studies focus on the tensile test properties of graded materials. With this approach, it is complicated to investigate the local material properties of the gradient and thus what the exact gradient in material properties is. Because of this, another measurement method is necessary. A widely used measurement method to analyze the local material properties of a heterogeneous material is nanoindentation. Through the measurements of the load and displacement, several properties, such as the reduced Young's modulus, can be measured. We can find many examples of measured composites in the literature, such as bone and teeth [72] and softer biological materials and polymers [73]. However, the measurements of soft biological material or soft polymers can be difficult. Difficult contact detection, the presence of high adhesion forces, and strong nonlinear behavior are reasons for this [74], [75]. Despite these challenges with this method, nanoindentation is still very well suitable for studying gradients in composite structures.

To create gradients, voxel-based 3D printing is a relatively new method. As said, with this technique, we can create gradients on a small length scale. A study has shown that nanoindentation can be applied to mechanically test a graded structure created with voxel-based 3D printing [61]. Mirzaali et al. [61] showed that a graded sample consisting of a hard and soft photopolymer could be tested through nanoindentation if one uses the right approach. However, their results showed that the gradient based on morphology does not result in the same gradient in material properties. A new strategy that creates a gradient based on the property and testing this through nanoindentation and a finite element analysis could open many new doors for designing graded bioinspired structures.

1.5. Objective of this research

As described above, a specific gradient in a hard-soft interface based on morphology does not result in the same gradient in material properties. To analyze the possibility of creating gradients based on a property, we will take advantage of the freedom allowed by voxel-based 3D printing. With this technique, we can precisely control the allocation of different materials within a structure and thus giving us exact control over the designed gradient in volume fractions. We base these volume fractions on a later introduced power-law function. This power-law function is a tool to obtain the functionality by design directly. We test this for several property functions, from which we obtained the initial data from our previous study that we performed in Liège [61]. The testing is done through nanoindentation. We will perform nanoindentation experiments to closely investigate how a created gradient will translate into the material properties of a graded composite. With this technique, we can closely measure the local material properties. This is necessary to determine if we achieved the expected functionality. We perform the nanoindentation experiments in two ways, through physical experiments as well as experiments through FEM. We will use the FEM to validate the experimental data and show that this is an excellent way to perform nanoindentation experiments when a physical nanoindenter is unavailable or desirable to test more designs.

The approach proposed here shows some advantages, such as precisely controlling the local outcome material properties. In this manner, we can tailor gradients to an expected functionality, which, in this case, is Young's modulus. In this way, we know the mechanical properties as well as the morphology of a gradient rather than only its morphology. With this new approach, better research on the toughness of different gradients can be performed, which is very useful for creating hard-soft interfaces that are both strong and tough. This approach can lead to interfaces that resemble more of those seen in nature, where the material is adapted directly to its function. Furthermore, the workflow proposed here uses nanoindentation as a parameter to identify the actual function that defines the property transition. This is in contrast with most studies, which focus on the tensile properties of graded material. To prove some of the advantages discussed here, we will apply our novel method in the design of a bioinspired graded model

Overall, we expect to create material properties by design while still improving overall properties with this approach. The algorithms we develop here for designing property-based functional gradients may be applied in a wide range of applications, such as soft robotics, flexural mechanism designs, 4D printing, multi-stable structures, and scaffold or implant design [76]–[79]. We can improve and tailor these examples to a specific applicational need in material properties by implementing the property-based functional gradients, and this could further enhance their performances and applications in the biomedical world.

1.6. Research questions

To evaluate if our approach has the desired outcome, several steps need to be taken to find answers to various research questions.

To create gradients by property designs, we first need to investigate if classic models such as the Halpin-Tsai model can correctly predict the material properties of bitmap printed gradients. If this is not the case, another approach is necessary. Therefore, we will first fit the Halpin-Tsai model to the earlier published data and determine if this model is accurate. We expect the model to be incorrect since it assumes parallel aligned fibers in the composite. In our designs, this is not the case because the hard and soft voxels are randomly scattered. Therefore, we expect that another approach is necessary.

The following substantial question is if the nanoindenter can successfully measure the whole range of Young's moduli in the gradient. It is necessary for the nanoindenter to correctly measure both the Young's modulus of the hard and soft material, and this can be challenging due to the earlier mentioned obstacles. If the nanoindenter is not able to do this, the results will not show the expected gradient. To investigate this, we will print a linear gradient in density and perform a nanoindentation experiment. We will then compare these results with the published data on a similar gradient [61]. Since, in the previously published study, we were able to measure the whole range of material properties, we expect this to be the same in this study.

As mentioned earlier, we will create a FEM based on nanoindentation experiments. In order to use this, we first have to assess if the FEM-based simulations can correctly predict the experimental data. To do this, we will create the FEM and perform an experiment on a linear gradient in density sample based on the earlier published data. We will compare the outcomes of this experiment with the earlier published data to determine if the model is working correctly. With the different parameters of the model correctly set, we expect that the FEM will correctly predict the experimental data.

After we have answered the questions above, we can start investigating our primary goal, which is to create gradients based on material properties rather than morphology. So, an important question is whether or not our workflow can correctly predict the outcome material properties of a particular gradient. In other words, do we see the gradient in material properties as we designed it? We will design different gradients based on the inverse of a function and test them through nanoindentation and Finite Element analysis to answer this question. Afterward, we will compare the results with the target gradient to assess if our workflow is successful. With the correct approach in the prediction model and testing, we expect that our workflow will accurately predict the material properties of a particular gradient.

When we have done this, we can look into the applications of our approach. In theory, graded structures will improve the material properties of more complex lattices. To investigate this, we will create a bioinspired model and test it with a tensile test. If our workflow is indeed correct, the graded sample will outperform its non-graded counterpart. If this is the case, we show that our findings are applicable in biomedical applications. As seen in literature, graded structures can significantly outperform non-graded ones. We expect this the be the same for our approach, possibly better.

Finally, we will draw an overall conclusion of the results to explore whether or not our workflow is complete or if something is missing. If something is missing, we can implement this in further research to further improve our approach. Although we have carefully prepared the workflow we present here, we expect to find ways to improve it further.

2. Methods

To achieve our objective, we need to follow several procedures. These include dealing with manufacturing and design, material characterization, experimental setup, and FE modeling setup. First, we have to create a control gradient. After this, we have to characterize our material, after which we can create our other designs, specify our way of testing the local material properties, and post-processing the data. Finally, we can create the FEM based on the experimental tests and characterize how to post-process the data.

2.1. Manufacturing and design

2.1.1. Stratasys J735

The printer used for the creation of the gradients is the Stratasys J735 from the company Stratasys. The printer has a native resolution of a voxel size of 42x84 (μm) and a layer thickness down to 14 (μm) in high-quality mode. However, we use the high-speed mode for the samples here, which has a layer thickness of 27 (μm). The 3D printer can print up to six different materials and two support materials using eight print heads. UV light solidifies the printed materials, which takes place after each printed layer. Because the curing happens after each printed layer, direct solidification occurs, ensuring continuous printing and firm adhesion between the voxels of the different materials [80].

The materials used for printing are that of the Vero and Agilus family from the company Stratasys. Vero is a rigid photopolymer with a Young's modulus of 2000 – 3000 (MPa) [81]. Agilus is a rubber-like photopolymer that is tear-resistant and can withstand repeated flexing and bending. The Young's modulus of Agilus is around 2 (MPa) [82].

2.1.2. Bitmap 3D printing

We used bitmap files as an input to print our designs. Bitmap printing uses images consisting out of black and white pixels to print different materials. It is possible to create several types of bitmaps, but we use the simplest 1-bit type in our case. This means that the black pixels have a value of 0 and the white pixels of 1. This creates a true/false statement for the 3D printer. In this way, the printer knows when to print a particular material. Since we use two materials in the designs, two sets of bitmap files are necessary. These two sets are the opposite of each other. One bitmap file is necessary for each to be printed layer. All these layers combined create the wanted sample (Figure 2). With MATLAB R2020a, we create a target gradient vector. Out of this target gradient vector, we create a gradient by calculating the number of hard material voxels per column and randomizing the locations of the voxels over this column. This randomization is done for every layer, resulting in a different bitmap file for each layer. However, the gradient and volume fraction per column are kept equal. All these layers combined create the overall sample.

2.1.3. Creation of control gradient

We created the different graded structures and their bitmap picture output files for the printer using MATLAB. These bitmap files are sent to the 3D printer using GrabCAD. The total size of the sample is 2.5 x 2.5 x 2.5 (cm). The sample consists of a hard border with a gradient inside it. The total size of the gradient is 1.5 x 1.5 x 2 (cm). These dimensions result in an overall size in voxels of 355 x 178 and 742 layers for the gradient and 591 x 296 and 742 layers for the overall sample. Figure 2 shows an example of the creation of a 3D printed sample with its dimensions. We designed the rest of the gradients for this study in this sample which we will later test through nanoindentation. For the creation of the other designs, we use a particular power-law function. To do this, we first have to characterize the local material properties of our composite.

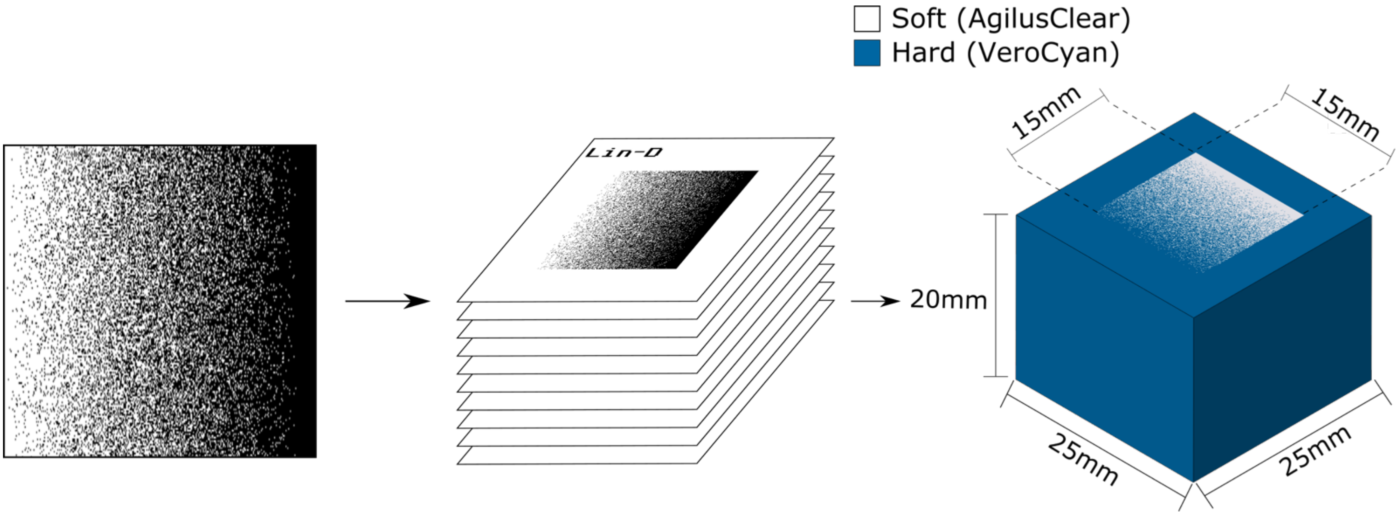

Figure 2: Schematic view of how the bitmap figures translate in the overall sample.-In the first two figures, white represents Vero and black Agilus. In the last figure, blue represents Vero and white Agilus.

2.2. Material characterization

We can define our composite as a particle reinforced composite. In this composite, the particles are randomly distributed and printed by a voxel-based approach. Most studies define a gradient based on morphology, resulting in difficulties for controlling the local material properties. Because of this setback, we created it as a function of mechanical property. In theory, earlier mentioned classical models, such as the Halpin-Tsai [83], should work to predict the Young's modulus of our composites. However, when we use the equation as mentioned earlier (equations 1 & 2) to predict the material properties of previously published particle voxel-based data that we tested using nanoindentation [61], it clearly shows that the prediction is incorrect (Figure 3). Figure 3 shows that the error between the Halpin-Tsai prediction and the experimental data is too high. However, when we make a comparison between the power-law regression in the form of:

$$E = a\rho^b$$

With a simplified b-value of 2, we observe that there is a small preliminary error. Because of the high error in the classical model and the power-law regression that shows a much lower error, a more comprehensive study on obtaining accurate a and b parameters is necessary.

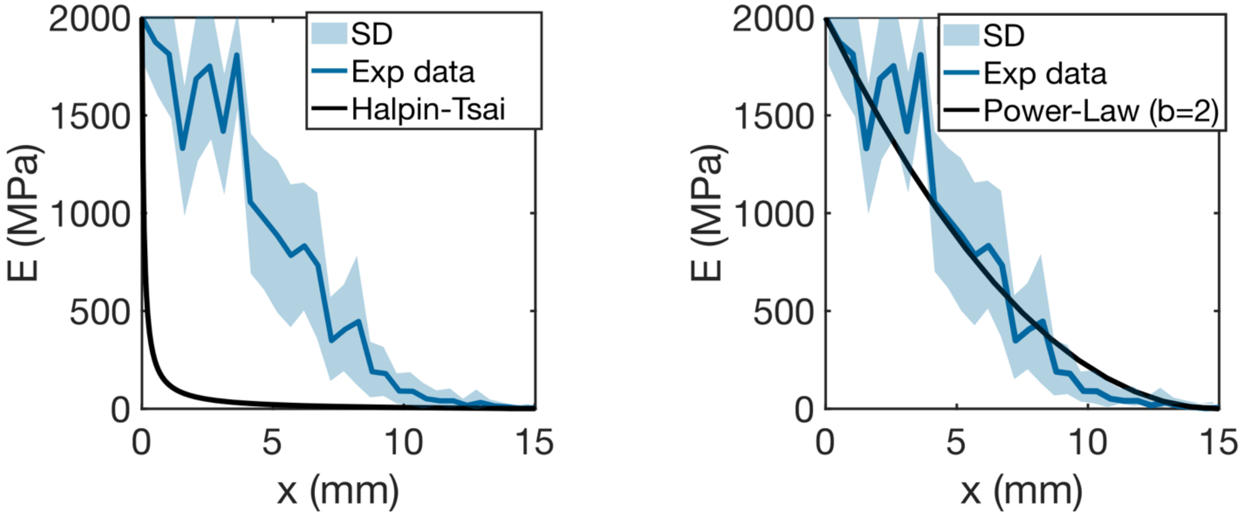

Figure 3: Left: prediction of elastic modulus based on the Halpin-Tsai model. The blue line represents the average of the previously published data [61], the blue shade the standard deviation of this data, and the black line the Halpin-Tsai prediction. Right: prediction of the elastic modulus based on the power-law function. The blue line represents the average of the previously published data, the blue shade the standard deviation of this data, and the black line the power-law prediction with a preliminary b-value of 2.

This research uses a power-law function to relate the hard material volume fraction with Young's modulus. We can use these power-law functions as a design tool for the gradient function. We use the inverse of this power-law function, which relates the soft-hard material ratio to specific material properties, as design parameters for the transition between two material phases. For these equations, we need the b parameter of our composite to design gradients since we know the material properties of the two materials.

We obtained this b-value in several ways. Three of them are: from experimental data of indentation tests, from heterogeneous indentation finite element model in small representative volume elements, and heterogeneous periodic boundary condition tensile finite element models in small representative volume elements. In this work, the focus lies on the first two.

The goal is to assess the accuracy of the different methods, which we did using the following steps: first, we create a control linear density transition. From this design, we perform the FEM tests and extract the b-value of the composite.

We based the control linear density function on a straight descending line (Figure 4B). After printing and testing this sample through nanoindentation, we can extract the b-value of our composite. We then implemented this b-value in the following equations to create the other designs based on material properties.

In global, for any b-value, we can follow these equations to define any gradient function of Young's modulus. In our study, we create a linear, stepwise, and sigmoid gradient. As we know, we have the power-law equation with the following shape:

$$E(x) = E_h \rho(x)^b + E_s \tag{5}$$

Wherein $\mathrm{E_h}$ is the Young's modulus of the hard material, in our case Vero, $\mathrm{E_s}$ the Young's modulus of the soft material, in our case Agilus, b the power-law coefficient, and $\mathrm{E(x)}$ and $\mathrm{\rho(x)}$ the overall Young's modulus and hard material volume ratio (*i.e.,* the hard material volume over the total volume of the composite) at their position x. We add $\mathrm{E_s}$ as we do not have a porous structure as happens typically with bone power-law and TPMS functions. Therefore, we can invert this to determine which $\mathrm{\rho(x)}$ we need to assign given a desired $\mathrm{E(x)}$ as:

$$\rho(x) = \left(\frac{E(x) - E_s}{E_h}\right)^{\frac{1}{b}} \tag{6}$$

Wherein $\mathrm{E(x)}$ is any function of Young's modulus between $\mathrm{x = 0\,(mm)}$ and $\mathrm{x = 15\,(mm)}$ as defined previously. Besides this, an important side note is that $\frac{\mathrm{E_s}}{\mathrm{E_h}} \approx 0$. Therefore, we can completely define any design after calculating b from the old exp data and the FE analysis. To corroborate the application of this hypothesis, we defined three functions of Young's modulus. These are a step, a sigmoid, and a linear function. Also, as for corroborating our b function from previous data, we reprinted and tested a control sample with a linear gradient in density. For the functions in Young's modulus, we defined them in the following way:

For the line, as it is a simple shape, we define the Young's modulus function as:

$$E_{lin}(x) = E_h - \frac{E_h}{15}x \tag{7}$$

Therefore:

$$\rho_{lin}(x) = \left(\frac{15E_h - E_h x}{15E_h}\right)^{\frac{1}{b}} = \left(\frac{15 - x}{15}\right)^{\frac{1}{b}} \tag{8}$$

We followed the same function of the line sample for the step, but we took steps from the line function and repeated them in z number of positions to obtain the desired steps.

For the design of the sigmoid function, we began by the definition of a sigmoid as:

$$E_{sig}(x) = \frac{E_h}{1 + exp\left(d\left(x - \frac{15}{2}\right)\right)} \tag{9}$$

Wherein d defines the slope of the exponential part of the sigmoid. For our design, we chose a value of $\mathrm{d} = 0.888$. So, for the density:

$$\rho_{sig}(x) = \left(\frac{E_h}{E_h \left(1 + exp\left(d \left(x - \frac{15}{2} \right) \right) \right)} \right)^{\frac{1}{b}} \tag{10}$$

Appendix A shows the lines of code to implement these equations for each of the gradient types in MATLAB.

After post-processing the data gathered from the previously published study [61], we fitted a line through this data based on the power-law and extracted the b-value of our composite (Figure 4B). The acquired b-value for these data is 2.027, which we rounded to 2.03 and used it for our studies

We created these designs in a way similar to the control gradient discussed earlier. However, with these designs, the target gradient vector is based on the equations explained above. In total, we created three new designs, which are a stepwise (Ste-E), linear (Lin-E), and sigmoid (Sig-E) gradient. Examples of the bitmap images of these designs and their respective expected Young's modulus and ρ functions are in Figure 4C**.** We printed these designs and experimentally tested them using a nanoindenter and with a FEM. From these results, we evaluate the accuracy of each design.

In the next chapter, we will describe the necessary procedures before the experiments and the experimental setup, and the post-processing of the experimental data. Furthermore, we will describe our modeling process and the post-processing of the data.

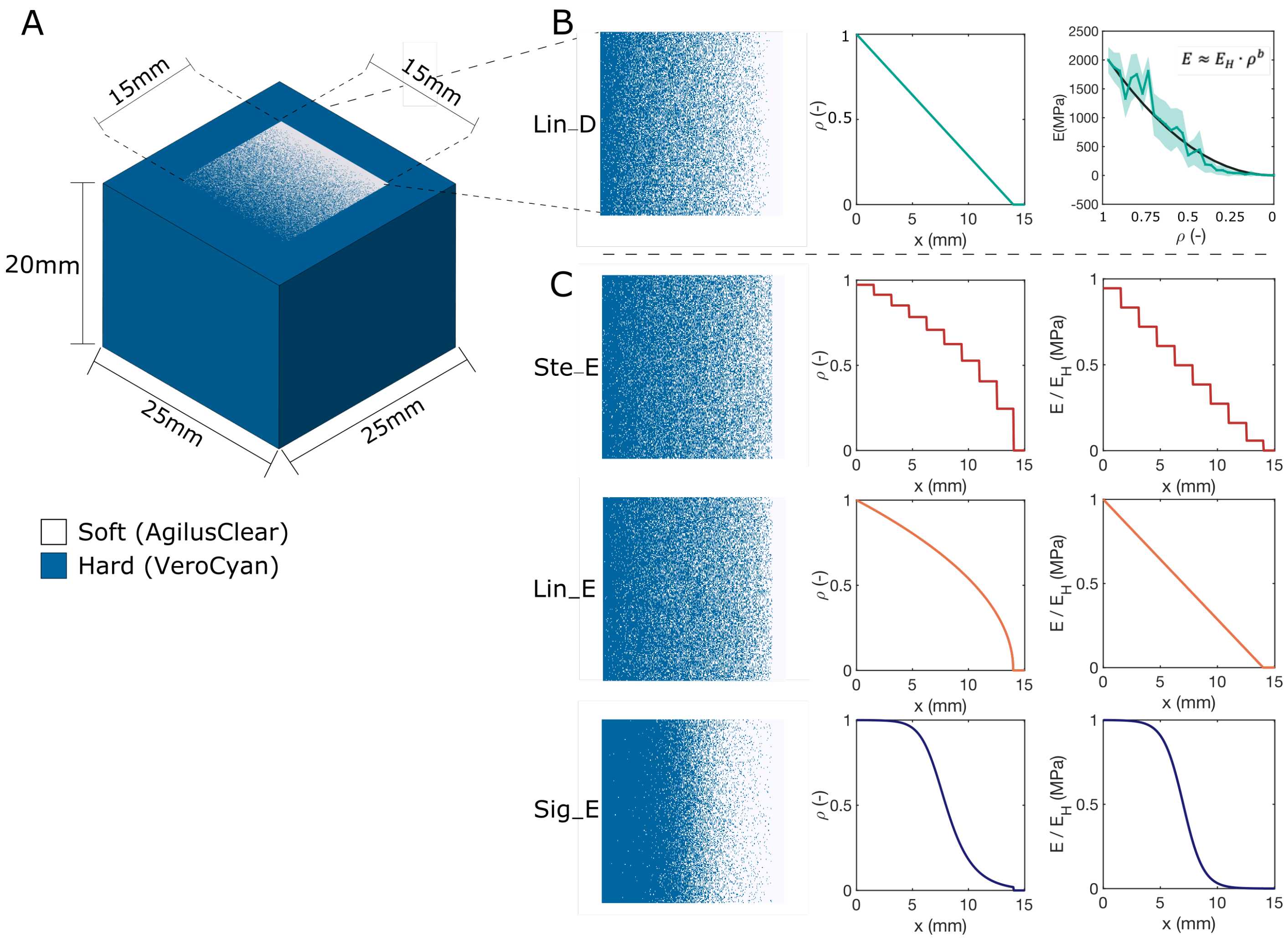

Figure 4: A) Schematic view of the dimensions of the design. B) Control linear-gradient, Lin_D, with D denoting a gradient based on density percentages. The first column shows an example of a bitmap file, the second column the created design, and the third column the measured data and fitted power-law (black line). C) The created stepwise (Ste_E), Linear (Lin_E), and sigmoid (Sig_E) gradients based on the power-law function, with E denoting that it is a gradient based on Young's modulus. The first column shows an example of a bitmap file, the second column the created gradient, and the third column the expected outcome gradient in Young's modulus.

2.3. Experimental setup

2.3.1. Sample pre-processing

After we printed the gradients, we polished them to smoothen the surface as much as possible. Studies have shown that the roughness of the surface of a sample can have a significant effect on the calculated Young's modulus. The reason behind this is that the roughness of the surface has a significant influence on the contact depth, and this contact depth is necessary to correctly calculate the Young's moduli of the material [84]. We made several polishing steps with a decrease in grain size every step to smoothen the sample's surface. We used an adjusted version of the Summet Method for Polymers of the company Beuhler, who makes the abrasive disks. In total, there were six steps (Table 1). We performed the polishing under constant hydration with a MetaServ 250 of the company Beuhler. After the polishing, we cleaned the samples using an ultrasonic bath to remove any diamond particles stuck to the surface, mainly to the Agilus. After this, we dried the samples with compressed air. We used compressed air to make sure that we damaged the polished surface as little as possible.

After polishing and cleaning, we inspected the samples with an optical microscope to control the polishing and check for any significant defects. Afterward, we stored the polished samples under a protective cover to prevent damage and avoid surface attachment.

Table 1: Polishing steps according to the Summet Method for Polymers of the company Beuhler (https://www.buehler.com/sumMet.php?material=Polymers).

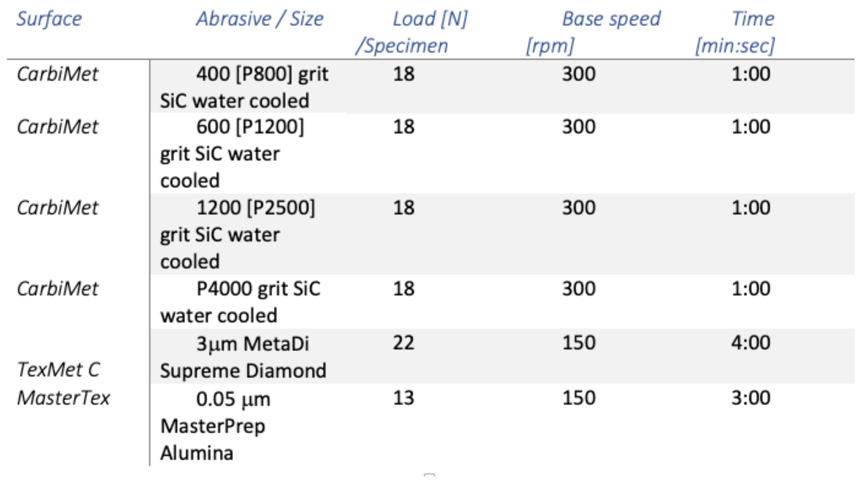

Surface	*Abrasive / Size*	*Load [N] /Specimen*	*Base speed [rpm]*	*Time [min:sec]*
CarbiMet	400 [P800] grit SiC water cooled	18	300	1:00
CarbiMet	600 [P1200] grit SiC water cooled	18	300	1:00
CarbiMet	1200 [P2500] grit SiC water cooled	18	300	1:00
CarbiMet	P4000 grit SiC water cooled	18	300	1:00
TexMet C	3µm MetaDi Supreme Diamond	22	150	4:00
MasterTex	0.05 µm MasterPrep Alumina	13	150	3:00

2.3.2 Experimental testing

We performed the experimental testing with the use of nanoindentation. For the measurements on the control gradient to acquire the b-value of our composite, performed in the previous study [61], we used the Hysitron TI 950 Triboindenter. We attempted to use the same setup as described in the previous paper for the measurements on the property-based designs; however, now we use the Piuma nanoindenter. There are some differences between these two nanoindentation machines, which we will describe in the following chapters.

2.3.2.1. Hysitron TI 950 Triboindenter

The nanoindenter used for the experiments is the Hysitron TI 950 Triboindenter of the company Bruker. The machine uses a diamond conospherical tip with a diameter of 20 µm. A diamond tip is necessary to assure that the compliance of the tip is less than that of the indented material [72]. A conospherical tip has the preference when indenting in polymers to reduce the chance of damaging the material when performing the indents [85]. Furthermore, the JKR calculation method used further on assumes a spherical tip [86]. We performed the indents in a grid with a spacing of 500 µm, resulting in a grid of 30 x 30 measuring points. Due to the adhesion effects present when indenting soft materials, we adopted a displacement-controlled load function. This is necessary to capture the whole interaction between the probe and the sample [61]. In this load function, the probe starts in contact at the surface, after which it retracts 2 µm above the surface. This is necessary to make sure the tip is out of contact with the surface of the sample. Here it is held for 10 seconds to ensure that if any adhesion was present, this is no longer the case. After these 10 seconds, it will move downwards for 3 μm, resulting in a 1 μm indent. Here again, it is held for 10 seconds. This waiting time makes sure the viscoelastic creep fades out before continuing the indentation [87]. After these 10 seconds, the probe retracts 3 μm. This is necessary to make sure the tip finishes the load cycle out of contact with the surface. This makes it able to mark the pull-off point. Both the downward and upward movements have a speed of 100 nm/s. Figure 5 shows a schematic view of this load function. A procedure like this makes it possible to quantify the adhesion effect. We do this by determining the jump-to-contact point and the pull-off force from the force-displacement data [61]. We further analyzed the force-displacement curves to calculate Young's moduli.

2.3.2.2. Piuma nanoindenter

The nanoindenter used for the newly created gradients is the Piuma nanoindenter from the company Optics11 Life in the Netherlands. The indenter uses a cantilever tip which differs from the Hysitron TI 950 Triboindenter, which uses a straight tip. Because of the tip shape, the cantilever must have the correct stiffness. If it is too stiff, there will be too little cantilever bending. If it is too soft, the indentation depth would be insufficient. The tip is a spherical tip made of glass with a size of 8 μm. The stiffness of the cantilever is 261 N/m. The total gird measured is 15 x 15 indentation points. We must first calibrate the stiffness of the cantilever to adjust for any offset in the cantilever and nonlinear response. This is necessary because the measurement point is not at the tip of the cantilever but the attachment site to the machine. After this calibration, we performed the measurements.

For this nanoindenter, we used a slightly different load function (Figure 5). In this load function, the tip moves downward for 15 μm, performing a 10 μm indent, where it is held for 7 seconds, after which it retracts 15 μm. With this machine, a bigger displacement is necessary to perform the indents. Furthermore, since this machine always starts 5 μm above the sample's surface, no retraction is necessary to ensure the tip is out of contact prior to the indentations.

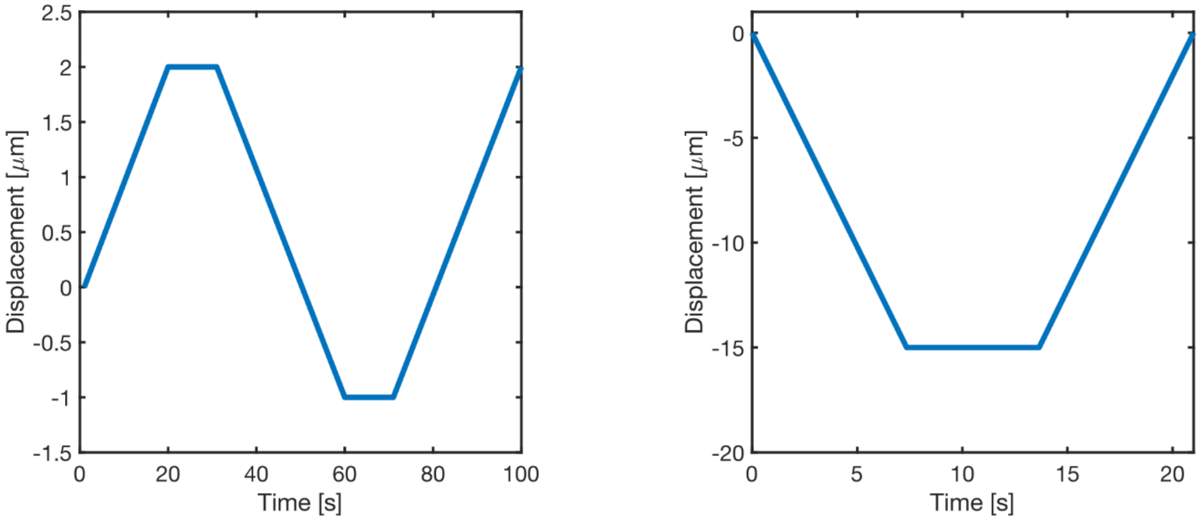

Figure 5: Displacement-controlled load function used for nanoindentation experiments with the Hysitron TI 950 Triboindenter (left) and Piuma nanoindenter (right)

2.3.2.3. Nanoindentation post-processing

After creating and preparing the samples according to the procedure mentioned before, we continued to test them through nanoindentation.

We tested the different samples in the following manner: first, we tested the control gradient (Lin-D) using the Hysitron TI 950 Triboindenter and the FEM to acquire the b-value of our composite in two different ways. For this sample, we measured 600 indentation points spaced in a 30 x 20 grid. From these results, we validated our FEM results and created the gradients based on material properties. We created four new gradients: one new control gradient (Lin-D) and three gradients based on our power-law function. These gradients are a linear (Lin-E), stepwise (Ste-E), and sigmoid (Sig-E). We use the Piuma nanoindenter to test these four gradients. Lin-D to validate the Piuma nanoindenter and the other three to test the approach presented in this study. For each of these samples, we measured 225 indentation points, spaced in a 15 x 15. The four gradients are also tested with the FEM to compare the resulting Young's moduli with the experimental data, which we will discuss later. We post-processed the nanoindentation data according to the following procedure.

For the calculation of Young's moduli measured with the nanoindenter, we used MATLAB rather than the machine's software. This is because the software of the nanoindenter is not well able to adjust for the adhesion forces. First, we visually analyzed all indents to remove any wrongly executed indents before further analysis with MATLAB. After this, we used two different calculation methods for the calculation of the local Young's moduli. If the adhesion force is higher than 5% of the maximum measured load, we analyzed the load-displacement curves with the Johnson-Kendal-Roberts (JKR) adhesion model [88]. This model uses the external force (F), contact radius (a), and indentation depth (δ) to calculate the reduced Young's modulus [89]. For the other curves, we used the Oliver-Pharr method [90]. Separation is needed because the adhesion force can overestimate the Young's modulus when the Oliver-Pharr method is used [88]. We zeroed the load-displacement curves for the load and displacement to capture the whole interaction between the tip and the sample, which is necessary to calculate Young's moduli of both methods correctly.

The JKR-method uses an exponential function, which is in-depth described by Ebenstein and Wahl [91]. We used this exponential function to fit the unloading in the force-displacement curve. The JKR-method uses the following exponential function [91]:

$$\delta - \delta_{contact} = \frac{a_0^2}{R}\left(\frac{1+\sqrt{1-\frac{P}{P_{adh}}}}{2}\right)^{\frac{4}{3}} - \frac{2}{3}\frac{a_0^2}{R}\left(\frac{1+\sqrt{1-\frac{P}{P_{adh}}}}{2}\right)^{\frac{1}{3}} \tag{11}$$

Wherein R is the indenter tip radius, P the measured force, P_{adh} the maximum adhesion force (Figure 7), and a_0 the contact radius between the probe and the sample (Figure 6) [91]:

$$a_0 = \left(\frac{9\pi R^2 \Delta\gamma}{2E_r}\right)^{\frac{1}{3}} \tag{12}$$

Wherein $\Delta\gamma$ is the work of adhesion, which measures the energy needed to pull the surfaces apart and E_r the reduced Young's modulus. We calculated $\Delta\gamma$ with the following equation [88]:

$$\Delta\gamma = \frac{-2P_{adh}}{3\pi R} \tag{13}$$

And E_r by [91]:

$$E_r = \frac{-P_{adh}}{2\pi R^2}\frac{(\delta_0 - \delta_{adh})}{3.3}^{-\frac{3}{2}} \tag{14}$$

Wherein δ_0 is the point where the unloading curve in the force-displacement graph crosses the x-axis, and δ_{adh} the displacement at maximum adhesive force (Figure 7). Equations 12, 13, and 14 can be implemented in equation 11 to fit the unloading curve of the indentation data. The variables a_0 (equations 12, 13, and 14) as well as P_{adh} (derived from the indentation data), are used as initial parameters for the curve fitting. With this fit, we can determine the reduced modulus with [88]:

$$E_r = \frac{-3RP_{adh}}{a_0^3} \tag{15}$$

P_{adh} as well as a_0 are outcomes from the fit. From this reduced modulus, we finally can acquire the real Young's modulus by [88]:

$$E_r = \frac{E}{(1-v^2)} \tag{16}$$

We used the Oliver-Pharr method for indentations where the adhesion force is less than 5% of the maximum measured force. The Oliver-Pharr method uses another equation to calculate the Young's modulus, which is the following [88]:

$$E_r = \frac{S\sqrt{\pi}}{2\sqrt{A(h_c)}} \tag{17}$$

Wherein $A(h_c)$ is the area function of the indenter tip restricted to 95% of the peak displacement (h_c) [88]:

$$A(h_c) = 2\pi R h_c - \pi h_c^2 \tag{18}$$

In equation 17, we calculated S by fitting the load-displacement curve. We used the following equation to fit the data [90]:

$$P = \alpha h^m \tag{19}$$

Wherein P is the measured load, h the displacement of the indenter and α and m constants. We used this equation to fit the data starting with initial values of α, δ_0 and m. We used the results of this fit to calculate S using the following equation [92]:

$$S = m\alpha(h_c - \delta_0)^{(m-1)} \tag{20}$$

By implementing the results of equations 18 and 20, we can calculate the reduced modulus for the Oliver-Pharr method with equation 17. From this, we can calculate the real Young's modulus using equation 16.
After we calculated the Young's moduli for all measurement points with the JKR and Oliver-Pharr method, we created a heatmap. After this, we averaged the values over every column to create a mean line of the indentation points in the x-direction with its standard deviation.

With the data extracted from the nanoindentation tests, we can generate heatmaps and plots using MATLAB. With these figures, we can compare the newly gathered Lin-D data to the previously published data [61] and those obtained from FEM for the same gradients. Furthermore, we can compare the data of the samples, with gradients based on mechanical properties, with their target gradient and the data gathered through FEM for these samples. Finally, we can use an R-squared rule criterion as an accuracy test between these processes to assess the reliability of our results.

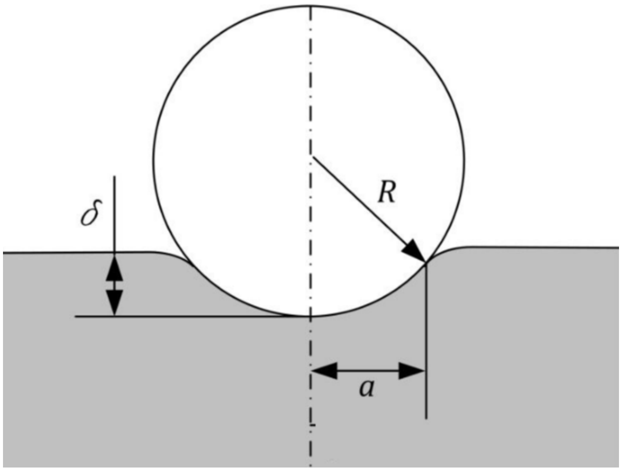

Figure 6: Schematic view of a spherical indentation tip wherein R is the indenter tip radius, a the contact radius, and δ the contact depth. Adjusted from Cheneler et al. [93].

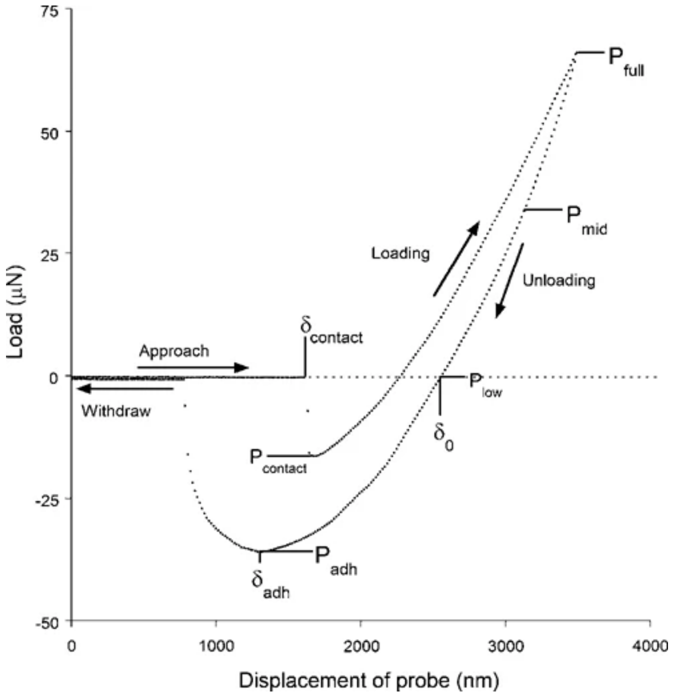

Figure 7: Schematic view of the load-displacement data showing the points used in the JKR calculation method. P_{adh} *is the maximum adhesion force,* δ_0 *the displacement where the unloading curve crosses the x-axis, and* δ_{adh} *the displacement at the maximum adhesion force. Take from Ebenstein [94].*

2.3.3 Finite element model setup

We created a Finite Element Model of the nanoindentation set up to validate the further gathered experimental data. Furthermore, we calculated the b-value of the power-law function for the control linear density transition and used it to corroborate the designs. We then compared this b-value with the b-value gathered through nanoindentation experiments on the same control linear density transition.

2.3.3.1. Nanoindentation model

With Abaqus, we created a Finite Element model out of the created gradients. In this model, we performed nanoindentation tests based on the experimental nanoindentation tests. We used representative volume elements (RVEs) to reduce the computational time. In Abaqus, we created separate models for each RVEs and performed a nanoindentation experiment on each. We created a grid of RVEs in the overall gradient with 15 indentation points in the x-direction and 9 in the y-direction (Figure 8B). Different parameters need to be set for these RVEs. These are the overall size of the RVEs and the size of the indenter tip. Besides these, we introduced another parameter in the model, which is a subdivision of the voxels. This subdivision is necessary to achieve better accuracy in the results since mesh conversion tests showed that the model's results depend on the mesh's size. After a series of conversion tests, which we further discuss in the results section (Figure 9), we set the number of subdivisions to 6 and the model's overall size to 6x6x6 voxels.

We used MATLAB to create the RVEs before they were implemented in the FEM using Python. With MATLAB, we separated the whole gradient into small RVEs of the earlier mentioned 6x6x6 voxels. This created 135 different files, one for each indentation point, which we then loaded into Abaqus, resulting in 135 different models.

The exact size for the voxels is similar to those of the used voxel-based 3D printer, which is 42 x 84 x 27 μm (Figure 8C). As said, we divided each voxel six times to increase the accuracy of the model. This gives a total of 50653 nodes and 46656 linear hexahedral elements of type C3D8R per model. We modeled the indentation tip as a 3D analytic rigid shell with a flat surface (Figure 8D). We performed four repetitions for each model to reduce the effect of the location of placement of the indenter. In these four repetitions, we randomized the placement of the indenter. However, we ensured that the indenter indents in the center of a voxel, and we excluded the outer ring of voxels as possibilities. We performed this exclusion to avoid any possible effects of the boundary conditions on the results. Furthermore, we kept the placement of the hard and soft unit cells the same. With the use of these repetitions, in total, we gathered 540 indentation points for each gradient.

We modeled the materials according to the used materials in the 3D printer. These materials are Vero as the hard material and Agilus as the soft. Both these materials are from the company Stratasys. For simplicity, we modeled Vero as an elastic material with a Young's modulus of 2000 (MPa). We measured the Poisson's ratio of Vero with an in-house tensile test and modeled it as 0.4. We modeled Agilus as an isotropic hyperelastic material. The model used for this is the Ogden material model. The values for the coefficients that we used in this model are μ_1=0.2497 (MPa), α_1=2.661 and D1 = 0.0602 (MPa^{-1}), where the expansion modulus D1 is equivalent to having a Poisson's ratio value of 0.49.

At the edges of the model and the bottom surface, there are encastre boundary conditions, which means that all displacements degrees of freedom of the model are zero. We modeled the indentation itself as a displacement in the z-direction of 1 μm (Figure 8). Out of the model, we extracted the force measured at the indenter tip and the displacement of this tip. We further processed this data using MATLAB.

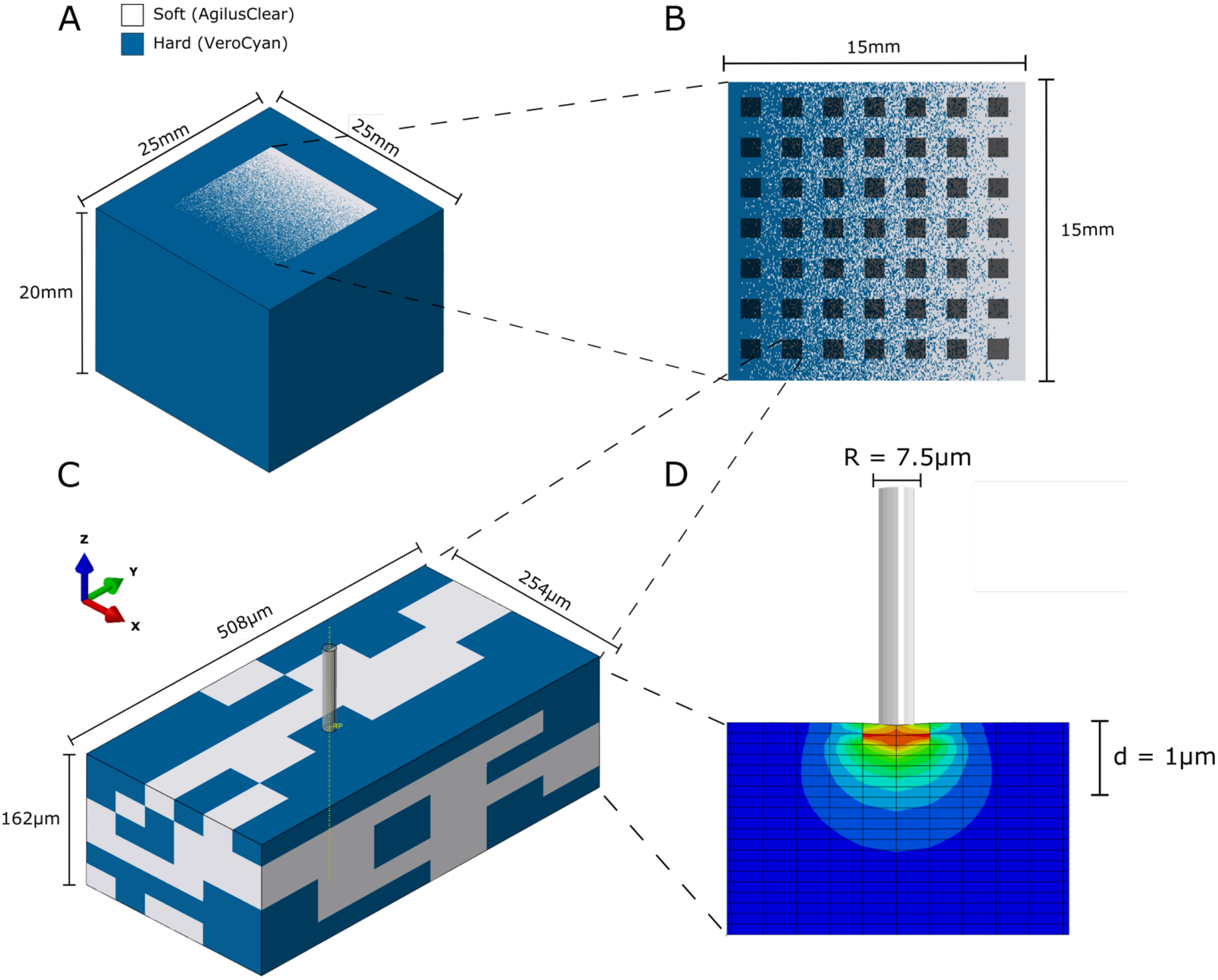

Figure 8: Details of the FEM wherein blue represents a hard voxel and white a soft. A) Schematic view of the dimensions of the overall design. B) Schematic view of the gradient dimensions, with, in white squares indications of RVE locations. C) View of the created RVEs with their dimensions. D) View of the indenter tip and its dimensions.

2.4.3.2. Finite element model post-processing

We further processed the data gathered from the FEM using MATLAB. Both the Oliver-Pharr and JKR methods use the force-displacement curve's unloading region to calculate the Young's modulus. Since the model shows an almost elastic behavior, the unloading region is the same as the loading region. Besides this, there is no adhesion force present in the FEM. Because of these two reasons, we adopted another calculation method to calculate Young's moduli for the FEM. For the calculation of the reduced Young's modulus (E_r) we used the following equation:

$$E_r = \frac{1}{\beta}\frac{\sqrt{\pi}}{2}\frac{S}{\sqrt{A_p(h_c)}} \tag{21}$$

Wherein $A_p(h_c)$ is the projected area of the indenter at an indentation depth h_c and β is a geometrical constant on the order of unity. Since:

$$S = \frac{dP}{dh} \tag{22}$$

Wherein P is the measured load and h the measured indentation depth. Furthermore, since we use a flat indenter $A_p(h_c)$ can be calculated with:

$$A_p(h_c) = \pi r_{ind}^2 \tag{23}$$

Wherein r_{ind} is the radius of the indenter probe. We can, in this case, rewrite this to:

$$E_r = \frac{S}{2r} = \frac{P}{2rh} \tag{24}$$

From the reduced Young's modulus, we can calculate the real Young's modulus with the following equation:

$$\frac{1}{E_r} = \frac{1-v_i^2}{E_i} + \frac{1-v_s^2}{E_s} \tag{25}$$

Wherein the subscript i means that it is a property of the indenter and the subscript s that it is a property of the specimen tested. Since the indenter in the model is rigid, we can rewrite this equation to:

$$E_s = E_r(1 - v_s^2) \tag{26}$$

With the use of equations 5 and 7, we can calculate the local Young's modulus. First, we calculated the Young's moduli for all 540 data points. After this, we averaged the four repetitions per model to calculate the Young's moduli for the 15 x 9 grid. Out of these points, we created a heatmap. After this, we averaged the rows for each column to create a mean line of the 15 indentation points in the x-direction, and we calculated the standard deviation. With this line, we can make a clear comparison between the theoretical gradient and the experimental data.

In the end, we compared the results of the different methods to see if they follow the target gradient line and, thus, if our method presented here is correct. We backed this up with an error function and R^2 tests. In this way, we can validate our models and our way of working.

3. Results and discussion

In this chapter, we will present and discuss the results. First, to validate the obtained b-value gathered through nanoindentation experiments performed in our previously published study [61], we ran our FEM based on the design used there. Therefore, we need to start this chapter with the convergence tests we performed to set the earlier mentioned parameters for the model. After this, we continue with a discussion about validating the power-law function of the earlier published data using our FEM. Hereafter, we will present the outcomes of the experimental and FEM nanoindentation tests of all the designs. This will be followed by an in-depth discussion about these results and an analysis of each design individually for both the experimental and FEM. After this, we present a biomimetic example of our property-by-design approach. Inside the ligaments of a knee joint 3D printed model, we implement a gradient which we then test and compare to a model without a gradient in the ligaments. We will compare the results to show if our approach will positively influence the overall material properties. Finally, we will give answers to the research questions presented in the introduction.

3.1. Parameterization Finite Element Model

As said, it is first necessary to perform convergence tests to set the correct parameters of our FEM. Figure 9 shows the different considerations for the parameters mentioned for the model. We have considered three primary parameters: the overall size of the RVEs, the size of the indenter tip (R), and the number of subdivisions of the voxels. We investigated the different parameters of the model using a model consisting of solely hard voxels with a Young's modulus of 2000 (MPa). In both figures A and B, it is visible that a model with 6x6x6 voxels shows the best results since those values are closest to the desired value of 1. To further investigate this, we selected the 6x6x6 voxel model and tested it for the different tip radii and different subdivisions (Figure 9C). In the model with a size of 6x6x6 voxels, there are three combinations of parameters closest to the desired value of 1. These are 2 subdivisions and a radius of 10 μm, 4 subdivisions and a radius of 5 μm, and 6 subdivisions and a radius of 7.5 μm. However, upon closer inspection on the exact values of E/E_h we can see that these values are 1.03, 0.9716, and 1.009, respectively. Because of this, we chose the combination of 6x6x6 voxels with 6 subdivisions and an indenter tip radius of 7.5 μm as parameters for the final model.

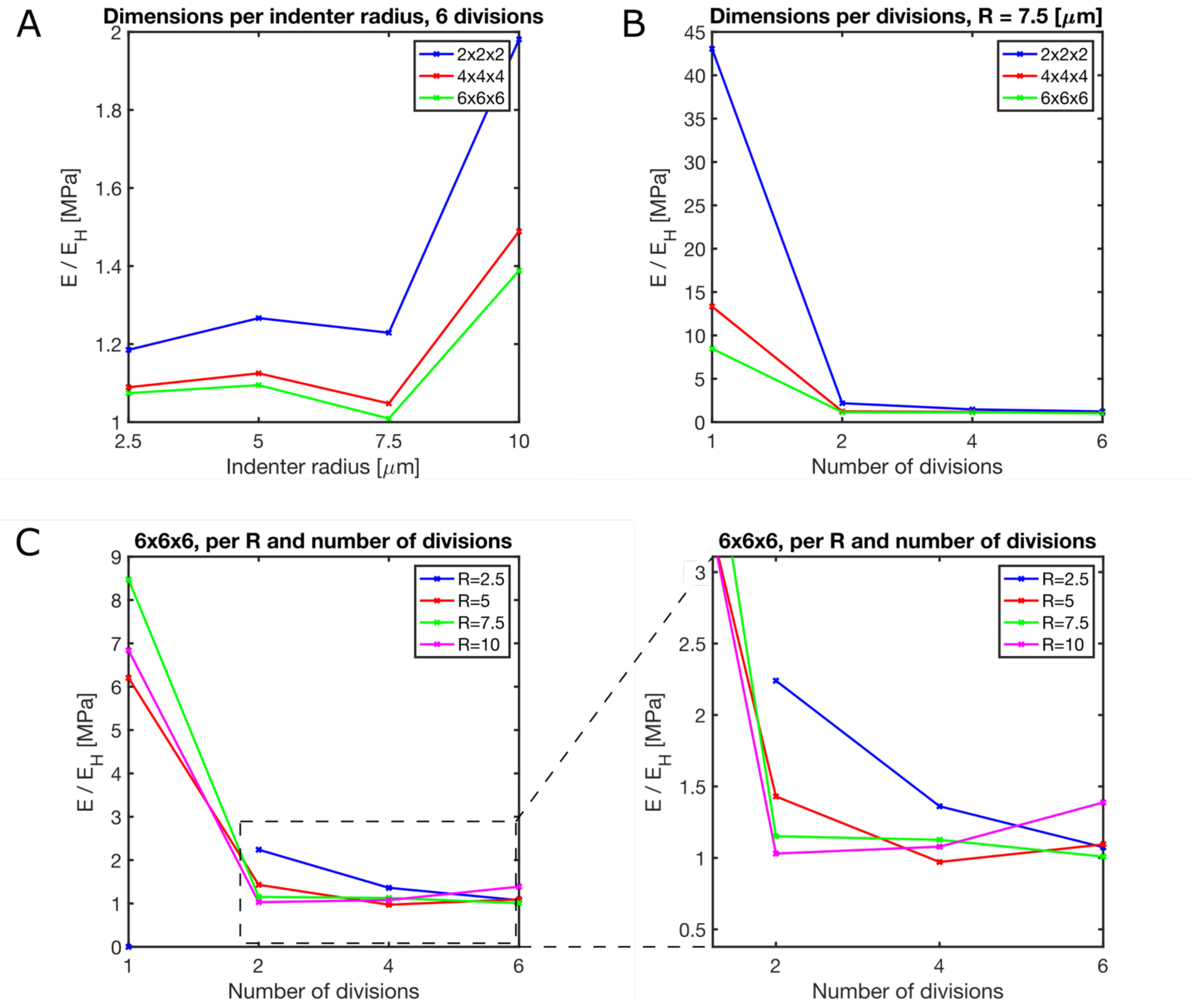

Figure 9: Figures showing the influence of the different design parameters of the FEM. The y-axis shows the measured Young's modulus divided by the Young's modulus of a hard voxel (2000 MPa). A) the influence of the dimension of the RVE per indenter tip size, with a fixed number of six subdivisions. B) Influence of the dimensions of the RVE per number of divisions, with a fixed indenter radius (R) of 7.5 (μm). C) Influence of the indenter radius per number of divisions, with a fixed RVE size of 6x6x6 voxels.

3.2. Validation of power-law function

As mentioned in the method section, we fitted a line through the previously published data and extracted the b-value, which was 2.027. However, we also performed a finite element analysis on that sample and similarly extracted the b-value for validation. Figure 10 shows the results for both the experimental data and the data gathered through FEM. The power-law fit gives a b-value of 2.03 for the FEM. Although the FEM shows an underestimation in the softer region and an overestimation in the higher region, and the experimental data shows some significant fluctuations, the fitted power-law functions come to almost the same b-value. This indicates that the fluctuations in both the FEM and experimental data result from statistical errors rather than measurements. Furthermore, since the b-values of the experimental and FEM data are similar, this indicates that the nanoindentation FEM is correctly describing the experimental nanoindentation experiment. This means that the FEM is working correctly, and we can use it to further investigate if our approach of creating property-based functional gradients is correct.

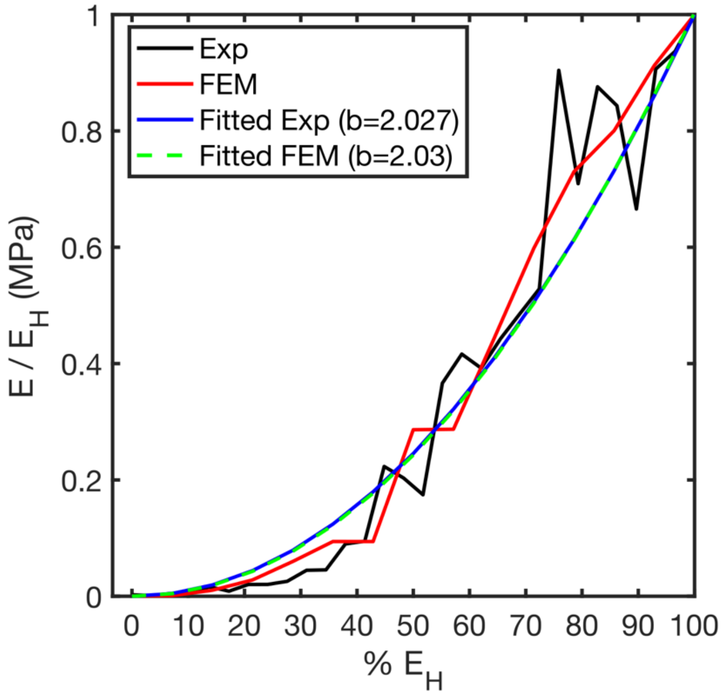

Figure 10: Comparison of b-values of the power-law function, for experimental and FEM indentation data, performed on a linear control gradient. The black line represents the experimental data gathered in the previous study, the red line FEM data based on the experimental data, the blue line the fitted power-law function on the experimental data with a resulting b-value of 2.027, and the green dotted line the fitted power-law function on the FEM data with a resulting b-value of 2.03.

3.3. Experimental and Finite Element results and discussion

After modeling and testing, we post-processed the data for both the experimental testing as well as the FEM and compiled the results (Figure 11).

Before we processed the experimental indentation data to calculate the Young's moduli, we first visually analyzed them to remove any wrongly performed indents. These wrongly performed indents can have several causes, for example, a small hole in the sample due to the printing or dust getting attached to the tip. For the four samples with a combined number of 540 indentation points, in total, we removed 17. 3 for Lin-D, 7 for Lin-E, 5 for Ste-E and 2 for Sig-E. These indentation points are visible as zeros in the heatmap. However, we excluded them in the calculation of the average lines in columns four and five of Figure 11.

After manufacturing and testing the designs, the FEM showed promising results, whereas the experimental data was not showing the gradients as expected (Figure 11). The experimental results, including the control design, do not follow the target lines (Figure 11E). However, in the lower values of Young's modulus, it is somewhat followed by the measured data. Only the stepwise gradient shows a line that is close to the target gradient. This is in contrast with the FEM data. The FEM samples do show gradients that are close to the target gradient. The R-squared values of the FEM data are all close to one, indicating that the data closely follows the target line, which is contrary to the experimental data. Here only the stepwise gradient shows an R-squared value close to one.

In the next part, we will discuss all the samples individually, and discuss the unexpected experimental outcomes and some essential points of the FEM results. Afterward, we will present our biomimetic application and give answers to the research questions.

We start by looking at the results of the control design (Figure 11E, Lin-D). The experimental data does not match the earlier published experimental data based on a similar sample. Of course, we do not expect that this gradient would follow the linear target gradient line, but it should follow the power-law function (black line Figure 11E). In the soft region, from around x=8(mm) to x=15(mm), it does follow the same trend as seen in the power-law function. Here we also see a very low standard deviation. In the harder region, x=0(mm) to x=8(mm), we start to see an increase in standard deviation, with a massive outlying point around x=6(mm).

This is also the region where the line starts to deviate from the expected shape. When we look at the, in theory, hardest point in the sample at x=0(mm), we see that this is not anywhere near the expected value of 1 (E/Eh). Overall, the line seems to follow a trend apart from the outlier at x=6(mm). However, this is not the trend that we would expect.

A similar problem is visible in the linear sample based on material properties (Figure 11E, Lin-E). Here again, in the soft region, x=10(mm) to x=15(mm), the results follow the expected line quite well with a low standard deviation. However, the data does not follow the target line in the harder region, x=0(mm) to x=10(mm), and the standard deviation increases. We can see three major outlying points. The first is at x=0(mm). Here the measured value is not anywhere near what we would expect it to be. The other two points are at x=4(mm) and x=8(mm). Here the values are higher than we would expect. The R^2-value is also very low for this design, indicating that the measured data does not follow the expected gradient.

There is an error in the measured values in the measured indentation data of both the Lin-D and Lin-E samples in the harder region of the gradient. This is also visible in the sigmoid gradient (Figure 11E, Sig-E). In this sample, in the region from x=6(mm) to x=15(mm), it does follow the target gradient quite well. However, there is an increase in standard deviation visible in this region. In the harder region, x=0(mm) to x=6(mm), some spikes are again visible, although they are less significant than in the linear samples. In the sigmoid gradient, the data does end in the hard region where we would expect it to end, at 1 (E/Eh). Also, the R-squared value is much closer to one, indicating that the data follows the target line more correctly.

Interestingly, the earlier mentioned problems are much less visible for the stepwise gradient (Figure 11E, Ste-E). There are some spikes present, but they are less severe. The gradient seems to follow the target gradient, although the standard deviation is relatively high throughout the gradient. The steps are not recognizable. Only at x=7(mm) and x=9(mm) can we see some stepwise behavior. The R-squared value is, therefore, the closest to 1 of all the experimental samples.

For all experimental samples, the heatmaps do not clearly show the created gradient (Figure 11C). This is particularly the case for the linear gradient samples. This is mainly a result of a few high outliers that shift the colors of the other points to a lighter color.

The issues with the experimental samples can arise from several factors. First, there could have been a problem with the printing and pre-processing of the samples. However, this is performed in the exact same manner as the previously published data, making it unlikely that this causes the error. Secondly, the load function of the indenter could be incorrect. With the Piuma nanoindenter, we used a shorter holding time than with the Hysitron TI 950 Triboindenter. Although studies show that it is possible to use a holding time in the range of 3 - 120 seconds and that the holding time can influence the measured value, a longer holding time would only result in higher measured values and would not explain the massive fluctuations [72], [95]. Thirdly, the error could arise from the post-processing of the data. However, we used the same method to post-process the previous data. Besides, we closely inspected the data gathered here to ensure it was adequately post-processed. It is most likely that the errors seen in the data here result from the used nanoindenter. As discussed earlier, the Piuma nanoindenter uses a cantilever tip. This type of nanoindenter is designed to measure the mechanical properties of soft and biological materials, while the Hysitron TI 950 Triboindenter uses a straight tip. For a cantilever tip, stiffness is critical for achieving accurate results. If it is too stiff, there will be too little cantilever bending. If it is too soft, the indentation depth would be insufficient. The range in Young’s modulus inside our gradient is relatively high (1 – 2000 MPa), meaning that it is challenging and possibly impossible, to have a tip with the correct stiffness to measure the whole range. Since the measured values are correct in the soft region and start to deviate in the harder regions, we can conclude that the tip we used was too compliant. Indenting with a lower indentation depth could enhance the measurements since a lower indentation depth expands the stiffness range of the tip. However, a minimum indentation depth is necessary to measure the material properties correctly.

The stepwise gradient does not quite follow this reasoning since this sample does seem to follow the gradient. However, the standard deviation is high in this sample. This could cause Young’s modulus line to average out correctly while the data gathered is not sufficiently accurate. A re-run of these experiments could show whether or not this is indeed the case or something else is causing the present issues.

The results showed that not all indentation machines are suitable for bitmap gradient testing and possibly other applications, especially where a significant difference exists between material properties. A nanoindentation machine with a straight tip with a stiffness much higher than the materials is necessary for these types of samples. Initially, we would test the samples with the Hysitron TI 950 Triboindenter. However, due to a defective machine as well as Covid, this was not possible. The samples will later be tested with this machine to prove that the approach presented here is correct.

Fortunately, we also performed a Finite Element analysis. Contrary to the experimental results, the results of the FEM do show the target gradient. To start with the linear gradient in density results (Figure 11D, Lin-D), we already showed in the validation of the b-value that the FEM results for this design are similar to the experimental data gathered through nanoindentation in our previous study. We still see some quite significant standard deviations. The reason for this is that the measured Young's modulus through nanoindentation greatly relies on the location of the indent. When, by chance, the indenter hits more soft or more hard voxels than expected in a particular column, this will clearly be visible in the results. As said earlier, four randomly placed repetitions are used per model to minimize this effect. However, even with these four repetitions in the simulations, this effect is still clearly visible. Ideally, one should use more indentation points in the y-direction and more repetitions to counteract this problem. However, this would take significantly more computational time while, in the end, the required results are already visible.

When we look at the linear gradient in material properties (Figure 11D, Lin-E) of the FEM, we see that the data follows the target gradient quite well. The R-squared value of 0.954 confirms this. However, there still are some fluctuations visible. Two major ones are at x=5(mm) and x=8(mm). The data follows the target line closely in the soft and hard regions, indicating that the algorithm works the best here. This is also visible in the stepwise gradient (Figure 11D, Ste-E). The stepwise overall seems to follow the target gradient, but it follows the target line the closest in the hard and soft region. However, there seems to be an overall overestimation in the middle section, and there are no clearly recognizable steps. Nevertheless, the R-squared value shows that the overall error is low.
The sigmoid gradient most closely follows the target gradient of all samples (Figure 11D, Sig-E). The R-squared value shows that there is almost a perfect fit. There are some minor outlying points visible, which are again visible in the middle section. However, they do not really influence the overall observed gradient.

For all gradients, the heatmaps show the created gradient quite well (Figure 11B). This is because, contrary to the experimental data, there are no high outliers present that shift the colors of the other points to a lighter color.

As said, the results of the stepwise gradient do not quite follow the recognizable steps that we created. It follows a more linear-gradient line. This is an artifact of the number of measure points used in the x-direction. At least two measure points per step should be used to see the steps clearly. We did this, and this is visible in Figure 12. However, the steps are still not fully recognizable. The fluctuations in the data points for the 30x9 model are even higher than with the 15x9 model. The earlier random placement of the indenter causes this. Increasing the measure points in the x-direction does not influence the model's accuracy at a point in x. So, the statistical fluctuations are still present, causing the results to not clearly show the created steps. Nevertheless, the error function shows that the error is low. This means that the measured points are close to the expected ones with the stepwise function.

Overall, we can distinguish some outlying points in all Finite Element samples and a sometimes high standard deviation. The random placement of the indenter and the random placement of the hard and soft unit cells are the reason behind this. The mean line of Young's modulus is the result of an average of many significantly different data points. In other words, the average is the result of heterogeneous behavior at the mesoscale. This is visible in Figure 12C and D. Here, we see the mean line of Young's modulus, with its standard deviation and all the separate measurement points in y-direction for both the FEM (15 points) and the old experimental data (30 points). Of course, the experimental has many more data points, but both measurement techniques still come to approximately the same outcome. Also, in the FEM graph, we can see that the spike at x=8(mm) results from two high outlying data points. This effect is the reason behind the higher fluctuations inside the middle regions than the hard and soft regions in all samples. When the unit-cells are more evenly separated into hard and soft, the chance that, in the four random repetitions, more hard than soft voxels, or the other way around, are indented is higher. This will result in more outliers and thus more spikes in the mean line. Of course, again, this could be solved by adding more points in the y-direction.

The FEM results shown here prove that it is an excellent method to study different gradients within a structure. The results already show a good representation of the target gradient, and, as explained, this would only improve with more data points. However, this technique is not limited to voxel-based gradients used here; one could also use it on reinforced gradients with different shapes and sizes. Right now, our model considers simplistic mechanics between the hard and soft materials, but it could be improved with, for example, viscoelastic behavior or different failure criteria. Future work should focus on this.

Overall, the results of our approach show that we can use nanoindentation to investigate gradients between hard and soft phases. However, one must use adequate machinery. A nanoindentation machine with a tip that is stiffer than the sample it has to indent is necessary. Nevertheless, even with a machine that is not well suitable for the type of testing performed here, the results of the softer region still show acceptable results, and the stepwise samples showed overall good results. The FEM showed much better results than the indentation data. When one creates a correct FEM with the correct parameters, it is a very viable method to study gradients. However, enough measurement points are necessary to achieve an excellent average result of the heterogeneous behavior of the mesoscale samples. Furthermore, the results we gathered show that our approach of applying a power-law function to a multi-material voxel-based 3D printed gradient is accurate enough to be used as a design tool to create gradients based on mechanical properties rather than morphology. For later studies, this design approach can be applied to several optimization methods to investigate the optimal design for the increase of toughness of a material. Furthermore, optimization methods can be used to only study homogeneous equivalents of these designs, which can be later discretized for 3D printing.

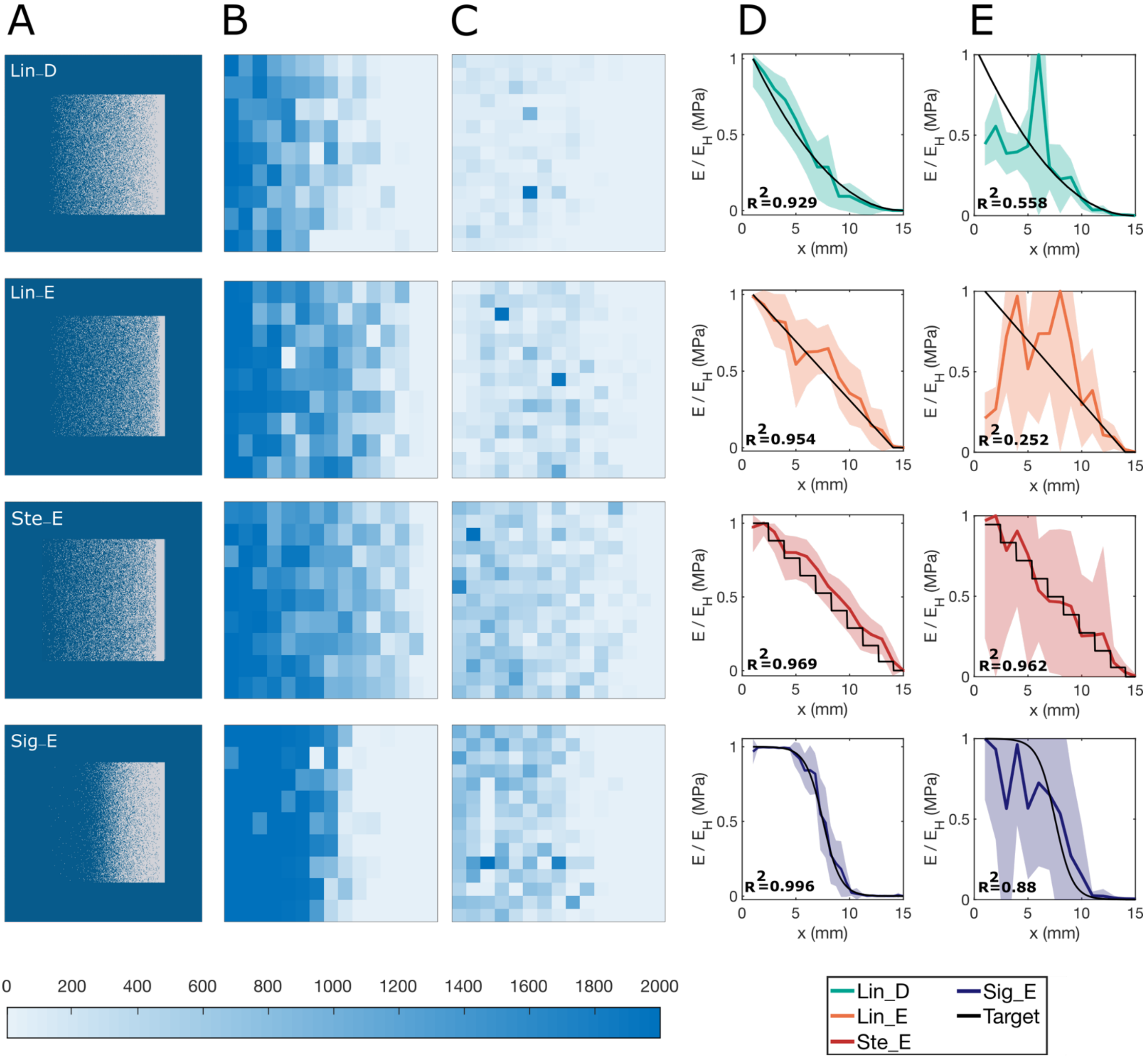

Figure 11: Results of the experimental and finite element indentation experiments. The first column shows the created designs. The first three letters show the created gradient and the last letter if it is created based on density percentage (D) or Young's modulus (E). The second column shows the heatmaps of the FEM data. This heatmap shows the measured Young's modulus of all the performed indentation points with the four repetitions averaged. The third column shows the heatmap of all the experimental data points. The fourth column shows the mean values per column compared to the target line (black) with the standard deviation as a shade of the FEM data. The fifth column shows the mean values per column compared to the target line (black) with the standard deviation as a shade of the experimental data. In both the fourth and the fifth column, the x-axis shows the distance on the sample and the y-axis the measured Young's modulus normalized.

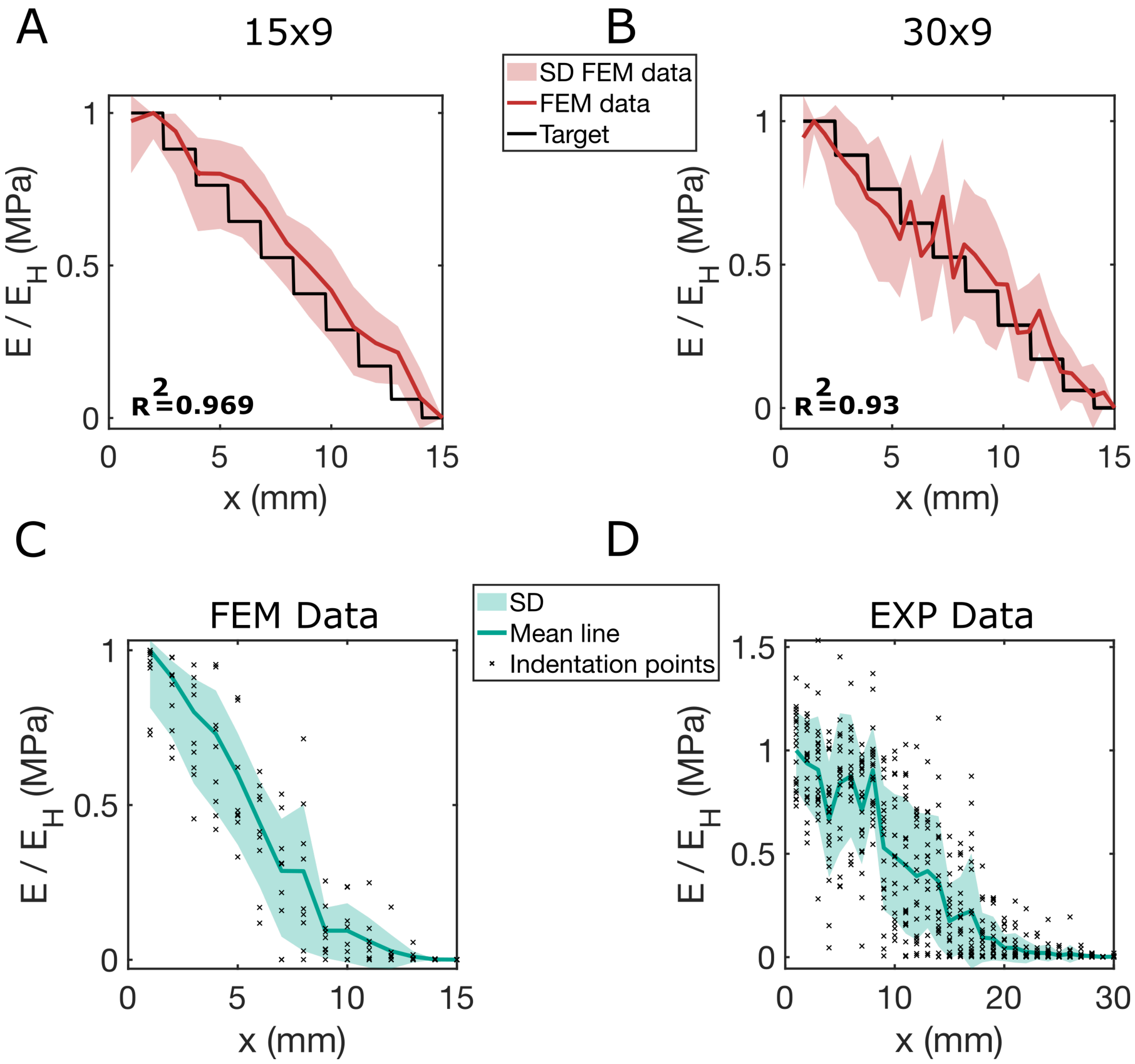

Figure 12: A) Stepwise gradient model with 15 measurement points in the x-direction and 9 in the y-direction. B) Stepwise gradient model with 30 measurement points in the x-direction and 9 in the y-direction. C), D) Figures of the average Young's modulus (green line), standard deviation (green shade), and every measure point in the y-direction (black x) for both the FEM (C) and experimental data (D) for Lin-D.

3.5. Bioinspired sample

After validating the earlier models and showing that our methodology works, we applied it to a biological example to extend our methodology. An excellent example of this is applying it to the knee's ligaments and testing it under tension to explore how much a gradient in the ligaments would increase the toughness. We created two 3D printed knee joint models—one without and one with gradients inside the knee's ligaments (Figure 13). We included the anterior cruciate ligament (ACL), posterior cruciate ligament (PCL), medial collateral ligament (MCL), and the lateral collateral ligament (LCL) in the model. We left the lateral and medial meniscus and the patella out since these are irrelevant for our study. We removed the three supports that are visible in Figure 13 & 14 before measurements. The total size of the created joint, including parts of the femur, tibia, and fibula, is 15cm. The total lengths of the ACL, PCL, MCL, and LCL are 2cm, 1.5cm, 3.5cm, and 3cm, respectively. We printed the femur, tibia, and fibula with Vero. We printed the ligaments with a combination of Vero and Agilus, based on the gradient from hard to soft material.

We tested the knee joint with a tensile test combined with a digital image correlation (DIC). DIC is an image analysis method that uses paint on a sample to measure the displacement and surface strains of a sample under tension. It does this in real-time in 3 dimensions. The software correlates the locations of pixels and the displacement of these pixels based on dots of paint. We measured the total force and displacement required before failure and captured the strains with the DIC. The DIC machine used is the Q-400 of the company Dantec Dynamics. Two digital cameras (12MP and CMOS chip) measure the surface strains, and two LED panels illuminate the samples. We loaded the samples with a quasistatic loading until failure. In order to correctly perform the experiments, we first have to calibrate the machine using a sample with a defined grid pattern. After this, we can perform the experiments. To get a high strain accuracy while keeping a low absolute strain error, we used a facet size of 33 x 33 pixels and a grid spacing of 11 pixels. The imaging frequency is 1 frame/sec. We performed the post-processing of the images and strain calculation with the Istra 4D x64 4.6.5 software of the company Dantec Dynamics. We will present the force-displacement and measured strain results, as well as a discussion about these results, in the next paragraph.

Figure 13: Posterior view of the 3D printed design of the knee joint after applying the black-dot speckle pattern for DIC testing.

3.5.1. Results for the bioinspired sample

Figure 14 shows the results of the DIC tensile test of both created knee designs. The force-displacement curves clearly show that the non-graded knee failed with half the energy than the graded one. Furthermore, we can also see that the overall maximum force was lower. The DIC images show that right before failure, the graded ligaments were loaded to the maximum strain of Agilus, which is reported to be approximately 95% strain. This is much higher than observed in the non-graded sample. In the force-displacement curves, we can also see that there are four drops in the measured forces. Failure of the ligaments causes these drops. The early failure in the non-graded knee is caused by the failure of the ACL. The underlying reason for this failure is a shear strain concentration in the bone to ligament interface. When adding a gradient to this ligament, we reduce this shear strain concentration and thus completely change the loading conditions of this ligament. Because we change this loading condition, the ligament can now act in tension instead of shear, leading to a much higher strain before failure. From these results, we can conclude that adding a functional gradient on a sample by itself already increases the overall toughness of a structure, which is in line with the results of previous research. However, the results also show that we can control the direction and function of the loading by adding gradients in different directions. Adding gradients based on a mechanical property function instead of morphology might allow future research to also predict stresses directly from image correlation results instead of only strains. This is because, by knowing the average value of Young's modulus for a section and having the experimental data of the strains, one can roughly identify the average strain of failure for a structure. From this, we can conclude that future research is necessary to explore these failure stress estimations and optimization analysis of homogenized models that we can later discretize into real properties.

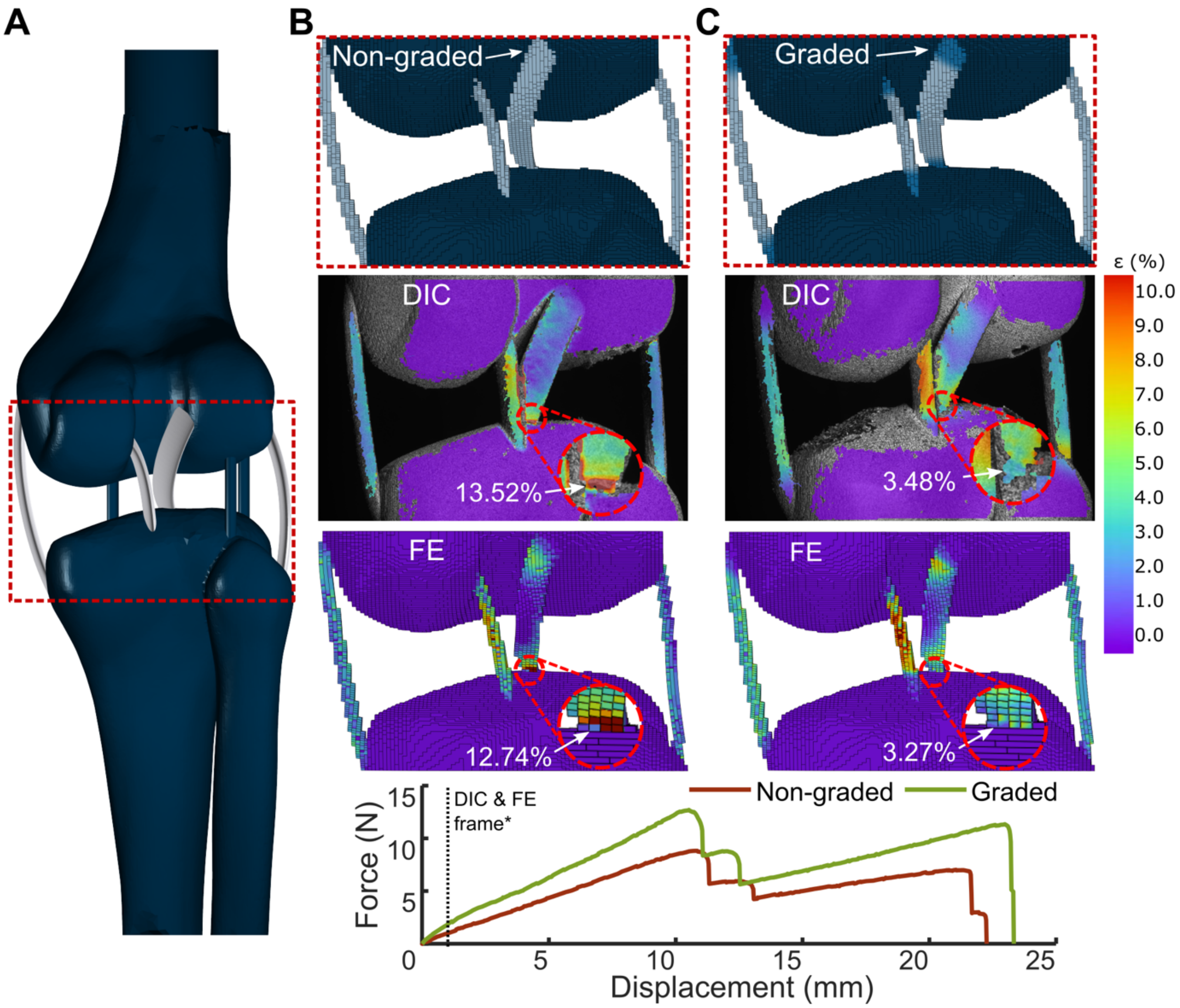

Figure 14: Results of the biomimetic knee design. A) The overall design of the knee, including the femur, tibia, fibula, ACL, PCL, MCL, and LCL. Blue represents Vero and white Agilus. B) Close-up of the non-graded ligament design and the DIC and FEM results showing the measured strain and forces. C) Close-up of the graded ligament design and the DIC and FEM results showing the measured strain and forces.

4. Conclusions

This research presents a new design approach to create gradients on mechanical properties rather than morphology. We did this by introducing a power-law function and creating different gradients based on this function and earlier gathered data. These newly designed gradients were then tested through nanoindentation and FEM to assess if our approach was correct. Finally, we applied our approach to a biomimetic sample to show an application of our findings. In the introduction, we have presented several research questions which we can now answer.

First, we had to investigate if the Halpin-Tsai model can accurately predict graded structures. Our results clearly show that the Halpin-Tsai model cannot correctly predict a bitmap-based 3D-printed composite's material properties. One of the main reasons for this is the one discussed earlier: it assumes parallel aligned short fibers. Because the Halpin-Tsai model was inaccurate, we had to apply another model in the form of a power-law function. This function showed much more accurate results, and we, therefore, used this model in the rest of the research.

After this, we had to assess if the nanoindenter could successfully measure the whole range of Young's moduli in our gradient. Contrary to our expectation, the nanoindenter used here was not able to do so. However, from the previously published data, combined with the data gathered through FEM, we can conclude that there are nanoindentation machines available that are able to measure the whole range. This shows that it is essential to choose a suitable machine for indentation experiments on these types of samples.

Fortunately, from comparing the gathered b-values, we can conclude that our FEM can accurately predict the experimental data. The b-value found through experimental data and FEM are similar, as well as both the average lines. However, the results of the parameterization analysis show that it is crucial to set the correct parameters to acquire accurate results. Furthermore, it is necessary to perform an adequate number of experiments to achieve a good average result of the heterogeneous behavior of the mesoscale sample.

Mainly from the results of the FEM, but also slightly from the experimental results, we can see that the outcome gradient in Young's modulus follows the target gradient in all of the samples. The experimental data did show some unexpected results. However, as discussed, this is caused by a problem with the indentation machine rather than an error in the workflow. Several other factors that could have caused the error in the results were discussed but are refuted. Using an indentation machine suitable for the type of samples used here will prove that the experimental data will also confirm our approach.

The biomimetic sample of the knee joints showed that introducing a gradient increases the energy to failure of the sample. Furthermore, we also showed that this introduction of the gradient would change the loading condition on the ligaments. From this, we can conclude that introducing a gradient itself will already increase the toughness and can also control the direction and function of the loading

Overall, the specimens presented here showed that, with our method, we could create a gradient based on material properties rather than morphology. Because of this, we can say that the objective of this research, to create a new approach to design gradients based on the precise deposition of hard-soft materials, is achieved. We achieved this by creating a FEM and validated this by performing nanoindentation tests. These tests showed that our approach was successful and that we can now design arbitrary functions to create functionally graded materials solely by controlling the hard volume fraction. This creates another level of freedom for the design of materials because we can now control the local stiffnesses. This has not earlier been done in the literature but is essential for further research. Applications to which this can be applied are numerous, for example, in controlling cell behavior, building in-vitro models, and bio-implants.
Future research could expand on the chosen approach by acquiring more indentation points for the Finite Element analysis, implementing optimization techniques, investigating the possibility to predict stresses directly from DIC results, exploring the possibilities to implement these methods of gradient designs in biocompatible designs, and applying it to other structures and shapes than voxels.

Bibliography

[1] R. O. Ritchie, 'The conflicts between strength and toughness', *Nature Materials*, vol. 10, no. 11, Art. no. 11, Nov. 2011, doi: 10.1038/nmat3115.

[2] D. R. King *et al.*, 'Extremely tough composites from fabric reinforced polyampholyte hydrogels', *Materials Horizons*, vol. 2, no. 6, pp. 584–591, 2015, doi: 10.1039/C5MH00127G.

[3] K. Lee, 'Effect of elastic modulus mismatch on the contact crack initiation in hard ceramic coating layer', *KSME International Journal*, vol. 17, pp. 1928–1937, Dec. 2003, doi: 10.1007/BF02982432.

[4] B. Liu, L. J. Huang, L. Geng, and F. Yin, 'Multiscale Hierarchical Structure and Laminated Strengthening and Toughening Mechanisms', 2018. doi: 10.5772/intechopen.69976.

[5] H. H. Lu and J. Jiang, 'Interface Tissue Engineering and the Formulation of Multiple-Tissue Systems', in *Tissue Engineering I*, K. Lee and D. Kaplan, Eds. Berlin, Heidelberg: Springer, 2006, pp. 91–111. doi: 10.1007/b138509.

[6] F. Barthelat, Z. Yin, and M. J. Buehler, 'Structure and mechanics of interfaces in biological materials', *Nat Rev Mater*, vol. 1, no. 4, pp. 1–16, Mar. 2016, doi: 10.1038/natrevmats.2016.7.

[7] F. Barthelat, H. Tang, P. Zavattieri, C. Li, and H. Espinosa, 'On the mechanics of mother-of-pearl: A key feature in the material hierarchical structure', *Journal of the Mechanics and Physics of Solids*, vol. 55, no. 2, pp. 306–337, Feb. 2007, doi: 10.1016/j.jmps.2006.07.007.

[8] F. Libonati and M. Buehler, 'Advanced Structural Materials by Bioinspiration: Advanced Structural Materials by Bioinspiration…', *Advanced Engineering Materials*, p. 1600787, Feb. 2017, doi: 10.1002/adem.201600787.

[9] L. Rossetti *et al.*, 'The microstructure and micromechanics of the tendon–bone insertion', *Nature Mater*, vol. 16, no. 6, pp. 664–670, Jun. 2017, doi: 10.1038/nmat4863.

[10] J. A. Trotter, K. Hsi, A. Samora, and C. Wofsy, 'A morphometric analysis of the muscle-tendon junction', *The Anatomical Record*, vol. 213, no. 1, pp. 26–32, 1985, doi: 10.1002/ar.1092130105.

[11] C. N. Maganaris and J. P. Paul, 'Tensile properties of the in vivo human gastrocnemius tendon', *Journal of Biomechanics*, vol. 35, no. 12, pp. 1639–1646, Dec. 2002, doi: 10.1016/S0021-9290(02)00240-3.

[12] S. Bekah, R. Rabiei, and F. Barthelat, 'The micromechanics of biological and biomimetic staggered composites', *J Bionic Eng*, vol. 9, no. 4, pp. 446–456, Dec. 2012, doi: 10.1016/S1672-6529(11)60145-5.

[13] C. N. Maganaris and J. P. Paul, 'In vivo human tendon mechanical properties', *J Physiol*, vol. 521, no. Pt 1, pp. 307–313, Nov. 1999, doi: 10.1111/j.1469-7793.1999.00307.x.

[14] K. S. Katti and D. R. Katti, 'Why is nacre so tough and strong?', *Materials Science and Engineering: C*, vol. 26, no. 8, pp. 1317–1324, Sep. 2006, doi: 10.1016/j.msec.2005.08.013.

[15] S. Mischinski and A. Ural, 'Finite Element Modeling of Microcrack Growth in Cortical Bone', *J. Appl. Mech*, vol. 78, no. 4, Jul. 2011, doi: 10.1115/1.4003754.

[16] E. Hamed, Y. Lee, and I. Jasiuk, 'Multiscale modeling of elastic properties of cortical bone', *Acta Mechanica*, vol. 213, pp. 131–154, Aug. 2010, doi: 10.1007/s00707-010-0326-5.

[17] F. Libonati, C. Colombo, and L. Vergani, 'Design and characterization of a biomimetic composite inspired to human bone', *Fatigue & Fracture of Engineering Materials & Structures*, vol. 37, no. 7, pp. 772–781, 2014, doi: 10.1111/ffe.12172.

[18] H. Bai *et al.*, 'Bioinspired Hydroxyapatite/Poly(methyl methacrylate) Composite with a Nacre-Mimetic Architecture by a Bidirectional Freezing Method', *Advanced Materials*, vol. 28, no. 1, pp. 50–56, 2016, doi: 10.1002/adma.201504313.

[19] Z. Jia and L. Wang, '3D printing of biomimetic composites with improved fracture toughness', *Acta Materialia*, vol. 173, pp. 61–73, Jul. 2019, doi: 10.1016/j.actamat.2019.04.052.

[20] C. Paul, 'Interface Property of Collagen and Hydroxyapatite in Bone and Developing Bioinspired Materials', p. 10, 2015.

[21] F. Libonati, A. K. Nair, L. Vergani, and M. J. Buehler, 'Mechanics of collagen–hydroxyapatite model nanocomposites', *Mechanics Research Communications*, vol. 58, pp. 17–23, Jun. 2014, doi: 10.1016/j.mechrescom.2013.08.008.

[22] K. J. Koester, J. W. Ager, and R. O. Ritchie, 'The true toughness of human cortical bone measured with realistically short cracks', *Nat Mater*, vol. 7, no. 8, pp. 672–677, Aug. 2008, doi: 10.1038/nmat2221.

[23] L. S. Dimas, G. H. Bratzel, I. Eylon, and M. J. Buehler, 'Tough Composites Inspired by Mineralized Natural Materials: Computation, 3D printing, and Testing', *Advanced Functional Materials*, vol. 23, no. 36, pp. 4629–4638, 2013, doi: 10.1002/adfm.201300215.

[24] M. Sedighi, N. Omidi, and A. Jabbari, 'Experimental Investigation of FGM Dental Implant Properties Made

from Ti/HA Composite', *MACS*, no. Online First, Jan. 2017, doi: 10.22075/macs.2017.1819.1096.

[25] A. Sadollah, A. Bahreininejad, H. Eskandar, and M. Hamdi, 'Optimum Material Gradient for Functionally Graded Dental Implant Using Particle Swarm Optimization', *AMR*, vol. 647, pp. 30–36, Jan. 2013, doi: 10.4028/www.scientific.net/AMR.647.30.

[26] M. M. A. Pratama, S. Abifurrizal, Y. Novitasari, W. Damayanthi, P. Puspitasari, and A. A. Permanasari, 'Potential use of graded concrete as structural elements of multi-storey buildings', *J. Phys.: Conf. Ser.*, vol. 1833, no. 1, p. 012040, Mar. 2021, doi: 10.1088/1742-6596/1833/1/012040.

[27] V. Bhavar, P. Kattire, S. Thakare, S. patil, and R. Singh, 'A Review on Functionally Gradient Materials (FGMs) and Their Applications', *IOP Conf. Ser.: Mater. Sci. Eng.*, vol. 229, p. 012021, Sep. 2017, doi: 10.1088/1757-899X/229/1/012021.

[28] N. Coomar and R. Kadoli, 'Comparative analysis of steady state heat transfer in a TBC and functionally graded air cooled gas turbine blade', *Sadhana*, vol. 35, no. 1, pp. 1–17, Feb. 2010, doi: 10.1007/s12046-010-0006-0.

[29] E. Bianchi *et al.*, 'Innovative Strategies in Tendon Tissue Engineering', *Pharmaceutics*, vol. 13, no. 1, p. 89, Jan. 2021, doi: 10.3390/pharmaceutics13010089.

[30] 'Grading of Aggregates in Concrete Spreadsheet', *CivilWeb Spreadsheets*. https://civilweb-spreadsheets.com/reinforced-concrete-design/grading-of-aggregates-in-concrete/ (accessed Sep. 24, 2021).

[31] M. Sadat-Shojai, M.-T. Khorasani, E. Dinpanah-Khoshdargi, and A. Jamshidi, 'Synthesis methods for nanosized hydroxyapatite with diverse structures', *Acta Biomaterialia*, vol. 9, no. 8, pp. 7591–7621, Aug. 2013, doi: 10.1016/j.actbio.2013.04.012.

[32] M. E. Launey, E. Munch, D. H. Alsem, E. Saiz, A. P. Tomsia, and R. O. Ritchie, 'A novel biomimetic approach to the design of high-performance ceramic–metal composites', *J. R. Soc. Interface.*, vol. 7, no. 46, pp. 741–753, May 2010, doi: 10.1098/rsif.2009.0331.

[33] S. Deville, E. Saiz, R. K. Nalla, and A. P. Tomsia, 'Freezing as a path to build complex composites', *Science*, vol. 311, no. 5760, pp. 515–518, Jan. 2006, doi: 10.1126/science.1120937.

[34] L. J. Bonderer, A. R. Studart, and L. J. Gauckler, 'Bioinspired Design and Assembly of Platelet Reinforced Polymer Films', *Science*, vol. 319, no. 5866, pp. 1069–1073, Feb. 2008, doi: 10.1126/science.1148726.

[35] H. Wei, N. Ma, F. Shi, Z. Wang, and X. Zhang, 'Artificial Nacre by Alternating Preparation of Layer-by-Layer Polymer Films and CaCO3 Strata', 2007, doi: 10.1021/CM062898I.

[36] P. Podsiadlo *et al.*, 'Ultrastrong and stiff layered polymer nanocomposites', *Science*, vol. 318, no. 5847, pp. 80–83, Oct. 2007, doi: 10.1126/science.1143176.

[37] B. Long, C.-A. Wang, W. Lin, Y. Huang, and J. Sun, 'Polyacrylamide-clay nacre-like nanocomposites prepared by electrophoretic deposition', *Composites Science and Technology*, vol. 67, no. 13, pp. 2770–2774, Oct. 2007, doi: 10.1016/j.compscitech.2007.02.007.

[38] D. Zhu and F. Barthelat, 'A Novel Biomimetic Material Duplicating the Structure and Mechanics of Natural Nacre', in *Mechanics of Biological Systems and Materials, Volume 2*, T. Proulx, Ed. New York, NY: Springer New York, 2011, pp. 181–187. doi: 10.1007/978-1-4614-0219-0_25.

[39] A. Sellinger *et al.*, 'Continuous self-assembly of organic–inorganic nanocomposite coatings that mimic nacre', *Nature*, vol. 394, no. 6690, pp. 256–260, Jul. 1998, doi: 10.1038/28354.

[40] J. D. Hartgerink, E. Beniash, and S. I. Stupp, 'Self-Assembly and Mineralization of Peptide-Amphiphile Nanofibers', *Science*, vol. 294, no. 5547, pp. 1684–1688, Nov. 2001, doi: 10.1126/science.1063187.

[41] N. A. Yaraghi and D. Kisailus, 'Biomimetic Structural Materials: Inspiration from Design and Assembly', *Annual Review of Physical Chemistry*, vol. 69, no. 1, pp. 23–57, 2018, doi: 10.1146/annurev-physchem-040215-112621.

[42] J. Wang, Q. Cheng, and Z. Tang, 'Layered nanocomposites inspired by the structure and mechanical properties of nacre', *Chem. Soc. Rev.*, vol. 41, no. 3, pp. 1111–1129, Jan. 2012, doi: 10.1039/C1CS15106A.

[43] I. F. Ituarte, N. Boddeti, V. Hassani, M. L. Dunn, and D. W. Rosen, 'Design and additive manufacture of functionally graded structures based on digital materials', *Additive Manufacturing*, vol. 30, p. 100839, Dec. 2019, doi: 10.1016/j.addma.2019.100839.

[44] E. L. Doubrovski, E. Y. Tsai, D. Dikovsky, J. M. P. Geraedts, H. Herr, and N. Oxman, 'Voxel-based fabrication through material property mapping: A design method for bitmap printing', *Computer-Aided Design*, vol. 60, pp. 3–13, Mar. 2015, doi: 10.1016/j.cad.2014.05.010.

[45] M. S. Reddy, R. Sundram, and H. A. Eid Abdemagyd, 'Application of Finite Element Model in Implant Dentistry: A Systematic Review', *J Pharm Bioallied Sci*, vol. 11, no. Suppl 2, pp. S85–S91, May 2019, doi: 10.4103/JPBS.JPBS_296_18.

[46] J. R. Singh, P. Kambalyal, M. Jain, and P. Khandelwal, 'Revolution in Orthodontics: Finite element analysis', *J Int Soc Prev Community Dent*, vol. 6, no. 2, pp. 110–114, 2016, doi: 10.4103/2231-0762.178743.

[47] A. Boccaccio, A. Ballini, C. Pappalettere, D. Tullo, S. Cantore, and A. Desiate, 'Finite Element Method (FEM), Mechanobiology and Biomimetic Scaffolds in Bone Tissue Engineering', *Int J Biol Sci*, vol. 7, no. 1, pp. 112–132, Jan.

2011.

[48] F. Barthelat, J. E. Rim, and H. D. Espinosa, ‘A Review on the Structure and Mechanical Properties of Mollusk Shells – Perspectives on Synthetic Biomimetic Materials’, in *Applied Scanning Probe Methods XIII*, B. Bhushan and H. Fuchs, Eds. Berlin, Heidelberg: Springer Berlin Heidelberg, 2009, pp. 17–44. doi: 10.1007/978-3-540-85049-6_2.

[49] I. Corni, T. J. Harvey, J. A. Wharton, K. R. Stokes, F. C. Walsh, and R. J. K. Wood, ‘A review of experimental techniques to produce a nacre-like structure’, *Bioinspir. Biomim.*, vol. 7, no. 3, p. 031001, Sep. 2012, doi: 10.1088/1748-3182/7/3/031001.

[50] O. Kolednik, J. Predan, F. D. Fischer, and P. Fratzl, ‘Bioinspired Design Criteria for Damage-Resistant Materials with Periodically Varying Microstructure’, *Advanced Functional Materials*, vol. 21, no. 19, pp. 3634–3641, 2011, doi: 10.1002/adfm.201100443.

[51] S. Fan and B. Yilong, ‘Mineral bridges of nacre and its effects’, *Acta Mech Sinica*, vol. 17, no. 3, p. 251, Aug. 2001, doi: 10.1007/BF02486881.

[52] F. Song, X. Zhang, and Y. Bai, ‘Microstructure and Characteristics in the Organic Matrix Layers of Nacre’, *Journal of Materials Research*, vol. 17, pp. 1567–1570, Jul. 2002, doi: 10.1557/JMR.2002.0233.

[53] Y. Yang *et al.*, ‘Electrically assisted 3D printing of nacre-inspired structures with self-sensing capability’, *Sci. Adv.*, vol. 5, no. 4, p. eaau9490, Apr. 2019, doi: 10.1126/sciadv.aau9490.

[54] T. Li, Y. Chen, and L. Wang, ‘Enhanced fracture toughness in architected interpenetrating phase composites by 3D printing’, *Composites Science and Technology*, vol. 167, pp. 251–259, Oct. 2018, doi: 10.1016/j.compscitech.2018.08.009.

[55] F. Libonati, G. X. Gu, Z. Qin, L. Vergani, and M. J. Buehler, ‘Bone-Inspired Materials by Design: Toughness Amplification Observed Using 3D Printing and Testing’, *Advanced Engineering Materials*, vol. 18, no. 8, pp. 1354–1363, 2016, doi: 10.1002/adem.201600143.

[56] M. C. McCorry, M. M. Mansfield, X. Sha, D. J. Coppola, J. W. Lee, and L. J. Bonassar, ‘A model system for developing a tissue engineered meniscal enthesis’, *Acta Biomaterialia*, vol. 56, pp. 110–117, Jul. 2017, doi: 10.1016/j.actbio.2016.10.040.

[57] A. J. Boys, J. A. M. R. Kunitake, C. R. Henak, I. Cohen, L. A. Estroff, and L. J. Bonassar, ‘Understanding the Stiff-to-Compliant Transition of the Meniscal Attachments by Spatial Correlation of Composition, Structure, and Mechanics’, *ACS Appl. Mater. Interfaces*, vol. 11, no. 30, pp. 26559–26570, Jul. 2019, doi: 10.1021/acsami.9b03595.

[58] D. Kokkinis, F. Bouville, and A. R. Studart, ‘3D Printing of Materials with Tunable Failure via Bioinspired Mechanical Gradients’, *Advanced Materials*, vol. 30, no. 19, p. 1705808, 2018, doi: 10.1002/adma.201705808.

[59] D. V. Kaweesa, D. R. Spillane, and N. A. Meisel, ‘Investigating the impact of functionally graded materials on fatigue life of material jetted specimens’, in *Solid Free. Fabr. Symp*, 2017, pp. 578–592.

[60] S. Hasanov, A. Gupta, A. Nasirov, and I. Fidan, ‘Mechanical characterization of functionally graded materials produced by the fused filament fabrication process’, *Journal of Manufacturing Processes*, vol. 58, pp. 923–935, Oct. 2020, doi: 10.1016/j.jmapro.2020.09.011.

[61] M. J. Mirzaali *et al.*, ‘Mechanics of bioinspired functionally graded soft-hard composites made by multi-material 3D printing’, *Composite Structures*, vol. 237, p. 111867, Apr. 2020, doi: 10.1016/j.compstruct.2020.111867.

[62] M. Loos, ‘Chapter 5 - Fundamentals of Polymer Matrix Composites Containing CNTs’, in *Carbon Nanotube Reinforced Composites*, M. Loos, Ed. Oxford: William Andrew Publishing, 2015, pp. 125–170. doi: 10.1016/B978-1-4557-3195-4.00005-9.

[63] E. Giner, V. Franco, and A. Vercher, ‘ESTIMATION OF THE REINFORCEMENT FACTOR ξ FOR CALCULATING E2 WITH THE HALPIN-TSAI EQUATIONS USING THE FINITE ELEMENT METHOD’, p. 8, 2014.

[64] P. R. Budarapu, X. Zhuang, T. Rabczuk, and S. P. A. Bordas, ‘Chapter One - Multiscale modeling of material failure: Theory and computational methods’, in *Advances in Applied Mechanics*, vol. 52, M. I. Hussein, Ed. Elsevier, 2019, pp. 1–103. doi: 10.1016/bs.aams.2019.04.002.

[65] E. F. Morgan, H. H. Bayraktar, and T. M. Keaveny, ‘Trabecular bone modulus–density relationships depend on anatomic site’, *Journal of Biomechanics*, vol. 36, no. 7, pp. 897–904, Jul. 2003, doi: 10.1016/S0021-9290(03)00071-X.

[66] J. H. Keyak, I. Y. Lee, and H. B. Skinner, ‘Correlations between orthogonal mechanical properties and density of trabecular bone: Use of different densitometric measures’, *Journal of Biomedical Materials Research*, vol. 28, no. 11, pp. 1329–1336, 1994, doi: 10.1002/jbm.820281111.

[67] J. C. Rice, S. C. Cowin, and J. A. Bowman, ‘On the dependence of the elasticity and strength of cancellous bone on apparent density’, *Journal of Biomechanics*, vol. 21, no. 2, pp. 155–168, Jan. 1988, doi: 10.1016/0021-9290(88)90008-5.

[68] I. Hvid, S. M. Bentzen, F. Linde, L. Mosekilde, and B. Pongsoipetch, ‘X-ray quantitative computed tomography: The relations to physical properties of proximal tibial trabecular bone specimens’, *Journal of Biomechanics*, vol. 22, no. 8, pp. 837–844, Jan. 1989, doi: 10.1016/0021-9290(89)90067-5.

[69] D. R. Carter and W. C. Hayes, ‘The compressive behavior of bone as a two-phase porous structure’, *JBJS*, vol. 59, no. 7, pp. 954–962, Oct. 1977.

[70] A. Kantaros, N. Chatzidai, and D. Karalekas, ‘3D printing-assisted design of scaffold structures’, *Int J Adv Manuf Technol*, vol. 82, no. 1, pp. 559–571, Jan. 2016, doi: 10.1007/s00170-015-7386-6.

[71] L. J. Gibson and M. F. Ashby, *Cellular Solids: Structure and Properties*, 2nd ed. Cambridge: Cambridge University Press, 1997. doi: 10.1017/CBO9781139878326.

[72] D. M. Ebenstein and L. A. Pruitt, ‘Nanoindentation of biological materials’, *Nano Today*, vol. 1, no. 3, pp. 26–33, Aug. 2006, doi: 10.1016/S1748-0132(06)70077-9.

[73] M. R. VanLandingham, J. S. Villarrubia, W. F. Guthrie, and G. F. Meyers, ‘Nanoindentation of polymers: an overview’, *Macromolecular Symposia*, vol. 167, no. 1, pp. 15–44, 2001, doi: 10.1002/1521-3900(200103)167:1<15::AID-MASY15>3.0.CO;2-T.

[74] A. S. Mijailovic, B. Qing, D. Fortunato, and K. J. Van Vliet, ‘Characterizing viscoelastic mechanical properties of highly compliant polymers and biological tissues using impact indentation’, *Acta Biomaterialia*, vol. 71, pp. 388–397, Apr. 2018, doi: 10.1016/j.actbio.2018.02.017.

[75] M.-G. Zhang, Y.-P. Cao, G.-Y. Li, and X.-Q. Feng, ‘Spherical indentation method for determining the constitutive parameters of hyperelastic soft materials’, *Biomech Model Mechanobiol*, vol. 13, no. 1, pp. 1–11, Jan. 2014, doi: 10.1007/s10237-013-0481-4.

[76] N. W. Bartlett *et al.*, ‘SOFT ROBOTICS. A 3D-printed, functionally graded soft robot powered by combustion’, *Science*, vol. 349, no. 6244, pp. 161–165, Jul. 2015, doi: 10.1126/science.aab0129.

[77] R. Tao *et al.*, ‘4D printed multi-stable metamaterials with mechanically tunable performance’, *Composite Structures*, vol. 252, p. 112663, Nov. 2020, doi: 10.1016/j.compstruct.2020.112663.

[78] D. Chen *et al.*, ‘4D Printing Strain Self-Sensing and Temperature Self-Sensing Integrated Sensor–Actuator with Bioinspired Gradient Gaps’, *Adv Sci (Weinh)*, vol. 7, no. 13, p. 2000584, May 2020, doi: 10.1002/advs.202000584.

[79] A. C. Daly, F. E. Freeman, T. Gonzalez-Fernandez, S. E. Critchley, J. Nulty, and D. J. Kelly, ‘3D Bioprinting for Cartilage and Osteochondral Tissue Engineering’, *Adv Healthc Mater*, vol. 6, no. 22, Nov. 2017, doi: 10.1002/adhm.201700298.

[80] J. Mueller, K. Shea, and C. Daraio, ‘Mechanical properties of parts fabricated with inkjet 3D printing through efficient experimental design’, *Materials & Design*, vol. 86, pp. 902–912, Dec. 2015, doi: 10.1016/j.matdes.2015.07.129.

[81] ‘Vero: A Realistic Multi-Color 3D Printing Material’, *Stratasys*. https://www.stratasys.com/materials/search/vero (accessed Jul. 18, 2021).

[82] ‘Agilus 30: A Flexible Photopolymer 3D Printing Material’, *Stratasys*. https://www.stratasys.com/materials/search/agilus30 (accessed Jul. 18, 2021).

[83] J. C. H. Affdl and J. L. Kardos, ‘The Halpin-Tsai equations: A review’, *Polymer Engineering & Science*, vol. 16, no. 5, pp. 344–352, 1976, doi: https://doi.org/10.1002/pen.760160512.

[84] J.-Y. Kim, J.-J. Lee, Y.-H. Lee, J. Jang, and D. Kwon, ‘Surface roughness effect in instrumented indentation: A simple contact depth model and its verification’, *Journal of Materials Research*, vol. 21, no. 12, pp. 2975–2978, Dec. 2006, doi: 10.1557/jmr.2006.0370.

[85] J. S. Field and M. V. Swain, ‘Determining the mechanical properties of small volumes of material from submicrometer spherical indentations’, *Journal of Materials Research*, vol. 10, no. 1, pp. 101–112, Jan. 1995, doi: 10.1557/JMR.1995.0101.

[86] J. K. Li, I. T. S. Li, G. C. Walker, R. M. A. Sullan, S. Zou, and Y. Sun, ‘7.19 - Polymer Nanomechanics’, in *Polymer Science: A Comprehensive Reference*, K. Matyjaszewski and M. Möller, Eds. Amsterdam: Elsevier, 2012, pp. 377–404. doi: 10.1016/B978-0-444-53349-4.00184-9.

[87] L. Angker, M. V. Swain, and N. Kilpatrick, ‘Characterising the micro-mechanical behaviour of the carious dentine of primary teeth using nano-indentation’, *Journal of Biomechanics*, vol. 38, no. 7, pp. 1535–1542, Jul. 2005, doi: 10.1016/j.jbiomech.2004.07.012.

[88] J. C. Kohn and D. M. Ebenstein, ‘Eliminating adhesion errors in nanoindentation of compliant polymers and hydrogels’, *Journal of the Mechanical Behavior of Biomedical Materials*, vol. 20, pp. 316–326, Apr. 2013, doi: 10.1016/j.jmbbm.2013.02.002.

[89] J. T. Pham, F. Schellenberger, M. Kappl, and H.-J. Butt, ‘From elasticity to capillarity in soft materials indentation’, *Phys. Rev. Materials*, vol. 1, no. 1, p. 015602, Jun. 2017, doi: 10.1103/PhysRevMaterials.1.015602.

[90] W. C. Oliver and G. M. Pharr, ‘An improved technique for determining hardness and elastic modulus using load and displacement sensing indentation experiments’, *Journal of Materials Research*, vol. 7, no. 6, pp. 1564–1583, Jun. 1992, doi: 10.1557/JMR.1992.1564.

[91] D. M. Ebenstein and K. J. Wahl, ‘A comparison of JKR-based methods to analyze quasi-static and dynamic indentation force curves’, *Journal of Colloid and Interface Science*, vol. 298, no. 2, pp. 652–662, Jun. 2006, doi:

10.1016/j.jcis.2005.12.062.

[92] K. Jha, N. Suksawang, D. Lahiri, and A. Agarwal, ‘Evaluating initial unloading stiffness from elastic work-of-indentation measured in a nanoindentation experiment’, *Journal of Materials Research*, vol. 28, pp. 789–797, Mar. 2013, doi: 10.1557/jmr.2013.3.

[93] D. Cheneler, N. Mehrban, and J. Bowen, ‘Spherical indentation analysis of stress relaxation for thin film viscoelastic materials’, *Rheologica Acta*, 2013, doi: 10.1007/s00397-013-0707-5.

[94] D. M. Ebenstein, ‘Nano-JKR force curve method overcomes challenges of surface detection and adhesion for nanoindentation of a compliant polymer in air and water’, *J. Mater. Res.*, vol. 26, no. 8, pp. 1026–1035, Apr. 2011, doi: 10.1557/jmr.2011.42.

[95] S. Yasin *et al.*, ‘Effect of experimental conditions on nano-indentation response of low density polyethylene (LDPE)’, *Journal of Macromolecular Science, Part A*, vol. 56, no. 7, pp. 640–647, Jul. 2019, doi: 10.1080/10601325.2019.1593791.

Appendix A

We used the following lines to implement the linear function in MATLAB:

```
X̄ = linspace(0,15,round(15/voxX))
ρ̄_lin= (1 - X/15 )'.^(1./b)
```

For the step, we used the line function and took steps from it and repeted them in `z` number of positions to obtain the desired steps. We then implemented this in MATLAB in vector shape as:

```
ρ̄_step= repelem(ρ̄_lin(1/10: round(15/(voxX*10)): end),10)
```

We implemented the sigmoid function in MATLAB using the following lines of code:

```
A = 4
D = 4 * A / 15
Z = 1 + exp(D.*(X-15./2))
ρ̄_sig= (1 ./ Z )'.^(1./b)
```

Wherein `A` is a parameter based on the desired slope of the sigmoid function.